Chemical Geology 533 (2020) 119435

Contents lists available at ScienceDirect

Chemical Geology

journal homepage: www.elsevier.com/locate/chemgeo

On the controls of mineral assemblages and textures in alkaline springs, Samail Ophiolite, Oman

Manolis Giampouras[a], Carlos J. Garrido[a], Wolfgang Bach[b,c], Catharina Los[b], Dario Fussmann[b], Patrick Monien[b], Juan Manuel García-Ruiz[a,*]

[a] Instituto Andaluz de Ciencias de la Tierra (IACT), Consejo Superior de Investigaciones Científicas–Universidad de Granada, Avd. Palmeras 4, 18100 Armilla, Granada, Spain
[b] Geoscience Department, University of Bremen, 28359 Bremen, Germany
[c] MARUM-Center of Marine and Environmental Sciences, 28359 Bremen, Germany

ARTICLE INFO

Editor: Karen Johannesson

Keywords:
Serpentinization
Alkaline springs
Carbonates
Mixing
Nesquehonite

ABSTRACT

Interactions between meteoric water and ultramafic rocks in the Oman Ophiolite generate waters of variable physicochemical characteristics. The discharge of these waters forms complex alkaline pool networks, in which mineral precipitation is triggered by mixing, evaporation, and uptake of atmospheric CO_2. A systematic and co-localized sampling of waters and solids in two individual spring sites allowed us to determine the saturation state of a range of minerals and correlate them to the different water and precipitate types. We subdivided the waters of the spring sites into three distinctive types: i) Mg-type; moderately alkaline ($7.9 < pH < 9.5$), Mg^{2+}–HCO_3^--rich waters, ii) Ca-type; hyperalkaline ($pH > 11.6$), Ca^{2+}–OH^--rich waters, and iii) Mix-type; alkaline to hyperalkaline ($9.6 < pH < 11.5$) waters with intermediate chemical composition. We first report the occurrence of hydrated magnesium (hydroxy-) carbonate phases in Mg-type waters. Nesquehonite forms in these waters via evaporation and transforms into dypingite and hydromagnesite under CO_2-rich conditions. In Ca-type waters, the coupling of atmospheric CO_2 uptake with evaporation leads to the formation of a calcitic crystalline crust on the air-water interface. The crusts are aragonite- and brucite-bearing, where Mg-type and Ca-type waters discharge and vigorously mix at the same pool. Unlike the Mg-type and Ca-type waters, the pools of Mix-type waters host massive aragonite-dominated deposits due to high Mg/Ca ratio that favors the growth of aragonite over calcite. The hydrodynamics during mixing spatially control brucite precipitation and restrict its formation and accumulation around specific mixing zones, where a continuous supply of Mg of inflowing Mg-type waters takes place. Crystal morphologies record the effect on the values of supersaturation and supersaturation rates in the pools due to mixing processes, evaporation and CO_2 uptake. In Ca-type waters, CO_2 uptake and evaporation dictate the textural characteristics of calcite both in crystalline crusts and rock coatings. Textural evolution of aragonite from crystalline sheaves to spheroidal shapes underlines the different supersaturation rates of calcium carbonate crystallization in flocculent material of Mix-type waters. Geochemical models of mixing between Mg-type and Ca-type waters revealed the evolution of mineral saturation indices under various mixing proportions, and their relation to the observed mineralogy and geochemistry of the pool waters. The thorough documentation of mineral assemblages and crystal morphologies enabled us to provide a more detailed account of how water composition, mixing, and mineral precipitation co-evolve in the alkaline spring systems, where CO_2 is sequestered.

1. Introduction

Serpentinization-driven processes have recently been identified to affect a vast range of environments on the Earth's (sub-)surface. These processes are highly relevant for currently debated issues, such as carbon capture and storage (Seifritz, 1990; Kelemen and Matter, 2008; Matter and Kelemen, 2009; Kelemen et al., 2011), the deep carbon cycle (Dasgupta and Hirschmann, 2010; Alt et al., 2013; Kelemen and Manning, 2015; Menzel et al., 2018, 2019), the origin of life (Martin and Russell, 2007; Martin et al., 2008; Lane and Martin, 2010; Sleep et al., 2011), and the detection of primitive life (García-Ruiz et al., 2003, 2017).

* Corresponding author.
E-mail address: juanmanuel.garcia@csic.es (J.M. García-Ruiz).

https://doi.org/10.1016/j.chemgeo.2019.119435
Received 18 March 2019; Received in revised form 22 November 2019; Accepted 27 November 2019
Available online 05 December 2019

Serpentinization is the process of hydrothermal alteration of peridotite and other olivine-rich rocks, producing particular geochemical environments under different geological conditions (e.g., Schrenk et al., 2013). Many studies have provided insights into the diversity of the fluid-rock interaction reactions leading to different mineralogical assemblages during serpentinization processes (Palandri and Reed, 2004; Bach et al., 2006; Frost and Beard, 2007; Klein et al., 2009; Klein and Garrido, 2011; Kelemen et al., 2011). Depending on the fluid and rock compositions, fluid-peridotite reactions at moderate to low temperatures result in the transformation of primary olivine and pyroxene, mainly into hydrous Mg-Fe-phyllosilicates (e.g. serpentine), magnesium hydroxide (brucite), Fe-oxides (e.g. magnetite), and Ca-Mg-carbonates (e.g. magnesite and calcite).

The Lost City hydrothermal field (LCHF) is a characteristic example of marine serpentinization and is hosted in an oceanic core complex (Atlantis massif) near the Mid-Atlantic Ridge at 30°N (Kelley et al., 2001). Fluids in LCHF show relatively low temperature (40–90 °C), high pH (9–11), high H_2/CH_4 ratio, and low metal concentrations (Kelley et al., 2005; Proskurowski et al., 2006). Active fluid venting leads to the formation of carbonate chimneys that consist of variable mixtures of calcite, aragonite, and brucite (Ludwig et al., 2006). In continental subaerial settings, serpentinization of ophiolites and subcontinental mantle peridotites by meteoric waters is typically linked to the formation of terrestrial alkaline spring systems (among others, in Oman: Neal and Stanger, 1985; Paukert et al., 2012, Chavagnac et al., 2013a, Turkey: Yuce et al., 2014; U.S.A.: Barnes et al., 1972; Blank et al., 2009; Morrill et al., 2013; Costa Rica: Sánchez-Murillo et al., 2014; Bosnia: Barnes et al., 1978, Cyprus: Neal and Shand, 2002, Italy: Bruni et al., 2002; Cipolli et al., 2004, Canada: Szponar et al., 2013; Portugal: Marques et al., 2008; and Spain: Etiope et al., 2016; Giampouras et al., 2020). There are also examples of mixed subaerial and subaquatic alkaline spring systems; Monnin et al. (2014) showed that serpentinization-affected meteoric water in Prony Bay (New Caledonia) discharges in a lagoon area, where it mixes with seawater forming carbonate concretions. In Aqua de Ney springs in California, Boschetti et al. (2017) suggested that the release of fossil seawater due to slab dehydration influenced the chemical profile of the hyperalkaline fluids before their discharge.

In terrestrial subaerial environments, the formation of the alkaline springs is the consequence of the infiltration and reactive percolation of meteoric waters in ultramafic rock aquifers. This process triggers numerous water-rock reactions that eventually lead to the generation of two distinctive types of waters, generally known as “Type I” and “Type II” waters (Barnes et al., 1967; Barnes and O’Neil, 1969). Type I waters are Mg^{2+}–HCO_3^--rich waters associated with shallow water flow paths in the ultramafic aquifer (Fig. 1), where waters are in equilibrium with the atmosphere and cause the chemical weathering of the host ultramafic rock minerals via reactions such as:

$$Mg_2SiO_4\ (\text{olivine}) + 4CO_2 + 2H_2O \rightarrow 2Mg^{2+} + 4HCO_3^- + SiO_2\,(aq) \quad (1)$$

Type II waters are Ca^{2+}–OH^--rich and their genesis requires deeper reactive percolation flow paths through the ultramafic bedrock (Fig. 1), where groundwater becomes isolated from the atmosphere triggering low-temperature serpentinization of olivine and pyroxene via reactions such as:

$$4Mg_2SiO_4\,(\text{olivine}) + CaMgSi_2O_6\,(\text{pyroxene}) + 7H_2O = 3Mg_3Si_2O_5(OH)_4\,(\text{serpentine}) + Ca^{2+} + 2OH^- \quad (2)$$

Type II waters are hyperalkaline (pH > 11) due to OH^- production during the dissolution of the host rock silicates (Palandri and Reed, 2004). The increase of the water pH could be supplemented by the concomitant OH^- and H_2 production during the oxidation of Fe^{2+} contained in the silicates to Fe^{3+} (Chavagnac et al., 2013a).

Studies of the terrestrial alkaline spring systems hosted in the Oman Ophiolite have provided a very detailed account of their geochemistry and mineralogy (69 sites in Neal and Stanger, 1983, 1984, 1985 and Stanger, 1986; 14 sites in Paukert et al., 2012; and 26 sites in Chavagnac et al., 2013a). These studies have identified the characteristic two water types previously described in terrestrial alkaline spring sites in ophiolites: moderately alkaline (pH = 7.5–9.5) Mg^{2+}–HCO_3^--rich (Type I), and hyperalkaline (pH > 11) Ca^{2+}–OH^--rich waters (Type II). The two water types mix upon their discharge and eventually form complex hydrological networks observed in different spring sites throughout the Oman Ophiolite (Fig. 1). Paukert et al. (2012) reported that these surface mixed waters are alkaline to hyperalkaline (pH between 8.5 and 11.9), showing variable Ca^{2+} (0.2 to 1.7 mmol L^{-1}), Mg^{2+} (0.02 to 2.5 mmol L^{-1}), and Dissolved Inorganic Carbon (DIC) (0.07 to 4.5 mmol L^{-1}) concentrations. In terms of their mineralogy, previous studies showed that calcium carbonate precipitation dominates the alkaline springs, while magnesium hydroxides are occasionally present. Hydromagnesite (Mervine et al., 2014), dypingite (Olsson et al., 2014) and layered double hydroxides (LDH) (Anraku et al., 2009; Chavagnac et al., 2013b) have been reported in some spring sites.

In submarine serpentinite-hosted alkaline systems, mixing of discharging alkaline fluids and seawater is the key driver of mineral precipitation (Kelley et al., 2005; Ludwig et al., 2006). In terrestrial alkaline spring systems, mixing of differently sourced waters may also, govern the precipitation and cause much of the geochemical and mineralogical diversity in the alkaline springs (e.g. Neal and Stanger, 1985; Paukert et al., 2012; Szponar et al., 2013; Chavagnac et al., 2013a, 2013b; Morrill et al., 2013; Leleu et al., 2016; Falk et al., 2016). A trademark of the Oman alkaline springs is the well-developed hydrological systems formed by the coeval production and, subsequent mixing, of hyperalkaline (Ca^{2+}–OH^- type) and moderately alkaline (Mg^{2+}–HCO_3^- type) water types (Neal and Stanger, 1985; Paukert et al., 2012; Chavagnac et al., 2013a).

In this study, we investigated two individual spring sites in the Oman Ophiolite, where mixing of the two water types is widespread and imposes a primary control of water composition and mineral precipitation. Although similar studies have been previously carried out in the Oman alkaline springs (Chavagnac et al., 2013a, 2013b), the present research complements these studies by providing a thorough documentation of the mineralogy, textures and crystal morphologies coupled to a conceptual geochemical and mineralogical mapping of the different pools in the spring sites. We conducted a systematic—downstream—sampling of waters and solids from numerous pools in the spring sites with the aim to examine the function of the spring sites under a geochemical, mineralogical and hydrodynamical perspective. The joint collection of water and solid samples from the same pool (each sampling point) allows us to determine the saturation state of a wide range of minerals and compare it to the mineralogy and (macroscopic and microscopic) textural features of the precipitates. This detailed pool-by-pool investigation enables us to provide an additional account of how water composition, mixing, and mineral precipitation co-evolve in the alkaline spring systems.

2. Geological setting and alkaline spring sites

The Samail Ophiolite (Sultanate of Oman and the United Arab Emirates) is one of the largest exposures of oceanic lithosphere on land and is composed of 12 distinct massifs lined up along the northeastern part of the Arabian plate (Fig. 2A). The ophiolites represent the topmost of a stack of nappes thrusted over autochthonous carbonate rocks (Hajar supergroup), which lie on top of a pre-Permian crystalline basement (e.g. Glennie et al., 1973; Coleman, 1981; Searle and Cox, 2002). The nappes consist of ~47 km of crustal rocks (layered gabbros, sheeted dikes, and volcanics) and ~10 km of variably serpentinized (~30–80%) upper mantle section (harzburgites and dunites) (e.g., Glennie et al., 1973; Coleman, 1981; Lippard et al., 1986; Nicolas et al., 2000; Godard et al., 2000; Monnier et al., 2006; Hanghøj et al., 2010).

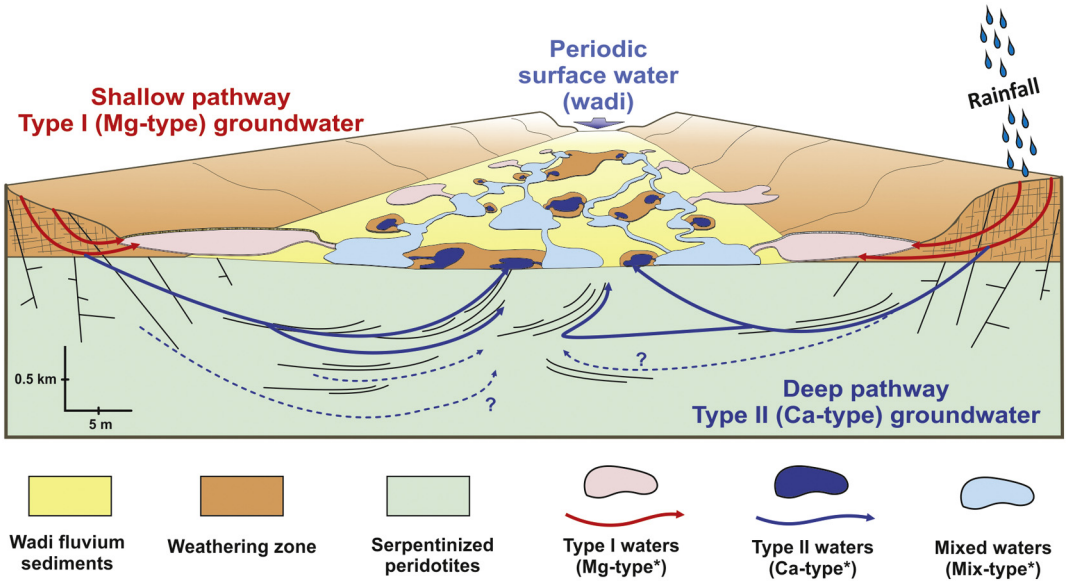

Fig. 1. Schematic illustration of the possible groundwater pathways and the different water types characterizing the spring systems. Modified after Mervine et al. (2014). Type I (red line) is CO_2-rich groundwater that follows near-surface pathways through the vadose zone and shallow fault systems. Deeper fluid percolation and isolation from the atmosphere leads to the formation of CO_2-depleted Type II groundwater (blue line). Mixing of these two waters upon discharge forms pools of mixed waters (light blue). Dashed lines show potential deeper water percolation in the peridotites. The horizontal scale represents only the frontal part of the sketch without taking into account the perspective of the image. *The terms "Mg-type", "Ca-type", and "Mix-type" are used in the present study to describe Type I, Type II, and mixed waters arising upon mixing of Type I and Type II waters, respectively. (For interpretation of the references to color in this figure legend, the reader is referred to the web version of this article.)

A large portion of the serpentine has probably formed during sub-oceanic hydrothermal alteration prior to the exposure of the ophiolites on land (e.g., Boudier et al., 2010). However, the partially serpentinized peridotites continue to experience on-going water-rock interactions at low temperatures (< 60 °C) (Neal and Stanger, 1985; Kelemen et al., 2011; Streit et al., 2012; Miller et al., 2016).

The present study focuses on two alkaline spring systems; the Nasif and Khafifah sites (80 km south of Muscat; Fig. 2C). Both sites are hosted in partially serpentinized ultramafic rocks from the Wadi Tayin massif (Fig. 2B), and they host a number of springs and water pools that form complex hydrological networks (Fig. 1). The first site (Nasif: 58°23′39.03″E, 22°53′43.23″N) is located NNW of Al Hayema town in wadi Nasif, and is hosted in partially serpentinized harzburgites of the mantle section that are highly fractured and weathered. The second site (Khafifah: 58°25′30.87″E, 22°54′14.23″N) is located N of Al Hayema town in wadi Khafifah (also known as Qafeefah). The Khafifah site is located at the end of the southeastern oriented wadi Khafifah and is placed in partially serpentinized harzburgites with minor dunite. However, the valley that hosts the Khafifah site represents an important tectonic boundary, as it separates harzburgites of the mantle section from gabbros belonging to the crustal section. In earlier communications, the Nasif site has been referred to as "Les Lauriers Roses" and the Khafifah site as "Rencontre de la Colombe" (Chavagnac et al., 2013a, 2013b).

3. Methods

3.1. Field methods

3.1.1. Sampling

We collected fifty-five (55) solid samples of fresh precipitates and lithified structures associated with alkaline and hyperalkaline waters that form the complex pool networks of the spring sites (Fig. 1). Thirty (30) water samples were taken from several pools and their contributors (spring outlets) by using 50 mL syringes (PE/PP), which were pre-rinsed with sample material. Sampling from deeper parts was conducted using a telescope sampling collector (Bürkle, Germany) equipped with a rinsed 500 mL polyethylene bottle. The waters from each sampling point were filtered through (pre-flushed) cellulose acetate membrane syringe filters (Sartorius Minisart Plus, pore diameter 0.45 μm) and directly filled into three different 10 mL polyethylene vials for alkalinity titration (pre-cleaned with ultrapure water, without headspace), trace metal analysis (pre-conditioned with distilled 5% HNO_3 and sample was fixed by adding 100 μL of distilled concentrated HNO_3), and anion analysis (pre-cleaned with ultrapure water).

The sites are characterized by active precipitation and sedimentation in the pools, as well as travertine terraces formed over the ultramafic rocks. We classified the collected solid samples according to their macroscopic features and spatial distribution into five types: i) Crystalline crusts floating on the water surface (Fig. 3A), ii) rock coatings around the pool rims (Fig. 3B), iii) flocculent material covering the bottom of the pool and/or being in suspension within the water column (Fig. 3C), iv) mud-like material forming dam-like formations (rippled terracing) and massive deposits within and adjacent to the pools (Fig. 3D), and v) lithified structures from active water flow areas (Fig. 3E) and travertine terraces (Fig. 3F). Lithified structures associated with active flow include dam-like formations and hardened concretions (Fig. 3E), whilst travertine terrace samples were collected from areas with no evident—at least currently—active flow.

3.1.2. In-situ measurements

Water samples were analyzed for pH, temperature, and electrical conductivity (EC) using a Hanna Instruments HI 98129 handheld tester, which was recalibrated daily. Alkalinity was directly measured in the field within 1 h after sampling. For this purpose, 10 mL of each sample was poured into a 20 mL polystyrene container under stirring, using a portable magnetic stirrer (IKA® Topolino Mobil). Under continuous stirring, 0.1 M hydrochloric acid (Titrisol, Merck, Germany) was added in 20–30 μL steps until a pH value between 3.5 and 4.3 was reached. The pH was monitored using a WTW Multi 3430 IDS portable meter, equipped with an IDS pH electrode (Sentix® 940) during the entire

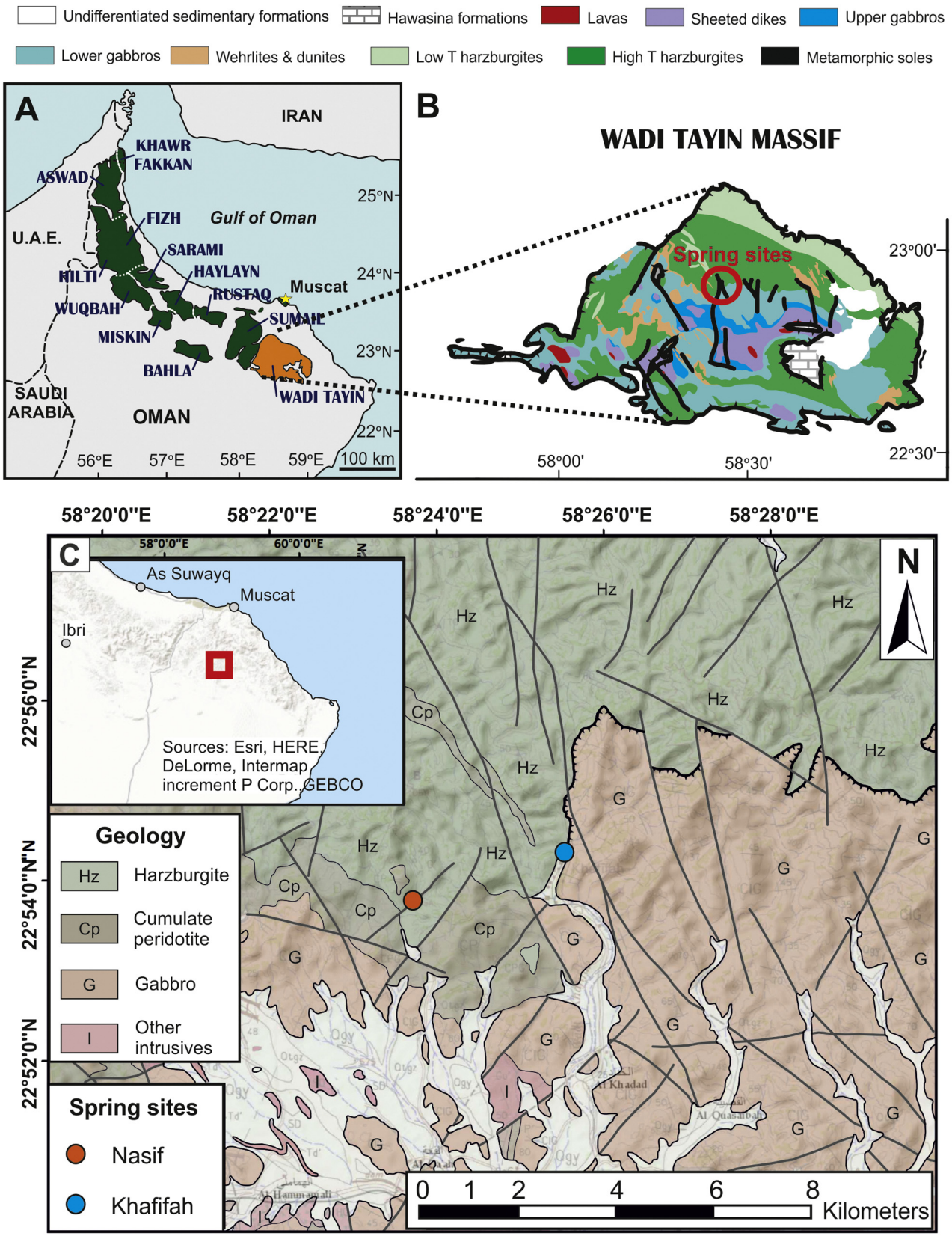

Fig. 2. Geology of the studied spring sites in the Samail Ophiolite, Wadi Tayin massif, Sultanate of Oman. A: The Oman Ophiolite (green) is located in the northeastern part of the Arabian plate and is composed of 12 large structural massifs (names indicated in blue). Modified after Godard et al. (2003). B: Geology of Wadi Tayin massif (orange in A), where the present study took place. The sampling sites, Nasif and Khafifah, are located within the red circle. Modified after Nicolas et al. (2000). C: Local geological map of the two spring sites, Nasif and Khafifah. Modified after de Gramont et al. (1986). (For interpretation of the references to color in this figure legend, the reader is referred to the web version of this article.)

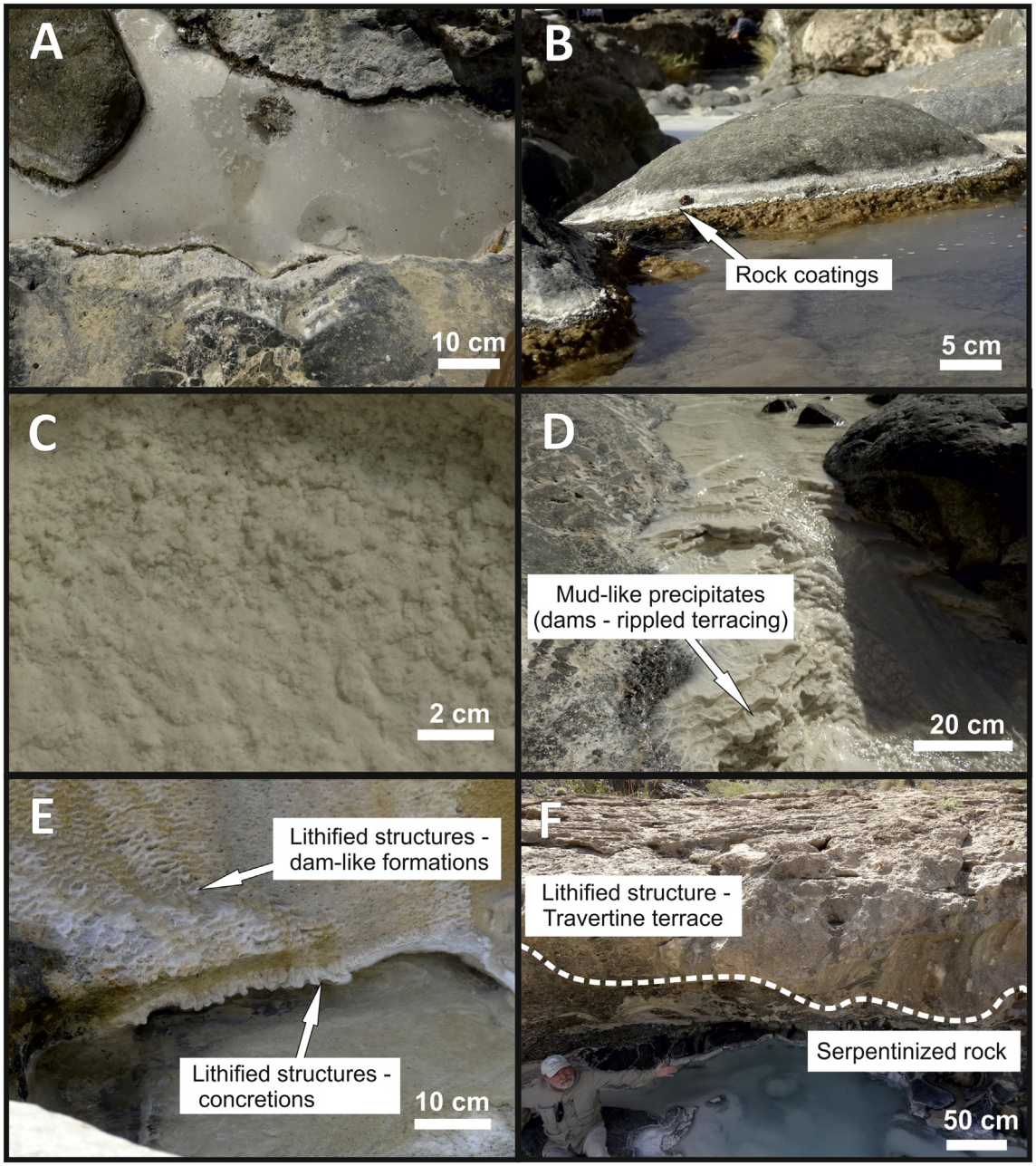

Fig. 3. Photographs of the types of the collected solid samples. A: Crystalline crusts floating on the water surface, B: rock coatings around the pool rims, C: flocculent material covering the pool bottom and/or being suspended in the water column, D: mud-like precipitates forming dam-like structures (rippled terracing) and massive deposits around streams and pools, E: lithified structures (dam-like formations and concretions) from active water flow areas and, F: travertine terraces lying on the ultramafic rocks.

alkalinity measurement process. Considering the change in the pH value and the volume of HCl added, the alkalinity can be calculated as:

$$Alk.\ (molL^{-1}) = [(V_{HCl} \times C_{HCl}) - 10^{-pHfinal} \times (V_0 + V_{HCl})/f_{H^+} + 10^{-\mathrm{pHstart}} \times (V_0/f_{H^+})]/V_0 \quad (3)$$

where V_0 represents the initial sample volume, V_{HCl} and C_{HCl} is the volume and the concentration of the added acid, pH_{start} symbolizes the initial pH value of the sample, pH_{final} is the final pH value after the end of the titration, and f_{H+} stands for the activity coefficient of H^+ ions (1.0 for freshwater). In order to determine the accuracy and the precision of the method, a 2.5 M $NaHCO_3$ solution was measured on a daily basis as a control. Precision was better than 0.5% and accuracy was < 3.3%. Dissolved inorganic carbon (DIC) was calculated using the following alkalimetric titration equation (Eq. (4)) given in Stumm and Morgan (1996):

$$C_T(molL^{-1}) = 1000 \times (Alk.\ /1000 + [H^+] - [OH^-])/(\alpha_1 + 2\alpha_2) \quad (4)$$

where C_T is the sum of the concentrations of carbonic species in the aqueous solution, and α_1, α_2 are the values of ionization fractions of carbonic acid. The ionization fractions were estimated using the equilibrium constants, $K_1 = [H^+][HCO_3^-]/[H_2CO_3]$ for HCO_3^- and $K_2 = [H^+][CO_3^{2-}]/[HCO_3^-]$ for CO_3^{2-}.

3.2. Analytical techniques

Water samples were analyzed for major (Ca, K, Mg, Na, Si) and trace elements (Ba, Sr) by inductively coupled plasma optical emission

Table 1
General sample information and physicochemical parameters of water samples.

Sample ID	Location	Coord.		pH	Temp	Cond.	Alk.
		Easting	Northing		(°C)	(μS cm^{-1})	(meq L^{-1})
Mg-type							
OM15-1W	Nasif	58°23′41.47″	22°53′44.20″	8.2	29.6	603	4.6
OM15-2W	Nasif	58°23′41.34″	22°53′44.11″	8.8	29.8	599	4.0
OM15K-2W	Khafifah	58°25′27.13″	22°54′16.93″	9.4	20.5	2705	15.5
OM15K-7W	Khafifah	58°25′27.24″	22°54′16.43″	8.2	20	640	5.5
OM15K-23W	Khafifah	58°25′31.27″	22°54′15.13″	9.3	24.1	455	2.6
Ca-type							
OM15-4W	Nasif	58°23′40.76″	22°53′43.99″	11.7	30.2	1183	4.1
OM15-9W	Nasif	58°23′40.38″	22°53′44.00″	11.6	32.2	1365	3.3
OM15K-1W	Khafifah	58°25′27.19″	22°54′17.10″	12	26.3	1710	5.4
OM15K-3W	Khafifah	58°25′27.28″	22°54′17.01″	12.2	20.1	1691	4.9
OM15K-4W	Khafifah	58°25′27.24″	22°54′16.92″	12.1	20.2	1560	4.9
OM15K-9W	Khafifah	58°25′27.36″	22°54′16.41″	11.9	28.4	1790	3.5
OM15K-11W	Khafifah	58°25′27.67″	22°54′16.37″	12.1	26.6	1724	5.8
OM15K-14W	Khafifah	58°25′28.19″	22°54′16.25″	12.1	25.4	1894	6.2
Mix-type							
OM15-3W	Nasif	58°23′40.77″	22°53′44.10″	11.2	30.2	890	1.3
OM15-5W	Nasif	58°23′40.65″	22°53′44.01″	9.5	29.4	610	3.8
OM15-6W	Nasif	58°23′40.56″	22°53′43.99″	9.7	29.3	614	4.0
OM15-8W	Nasif	58°23′40.39″	22°53′43.86″	10.5	29.9	630	2.1
OM15-11W	Nasif	58°23′39.56″	22°53′43.43″	10.7	29.2	642	2.0
OM15-12W	Nasif	58°23′39.03″	22°53′43.23″	10.5	26.9	595	1.9
OM15K-5W	Khafifah	58°25′27.21″	22°54′16.55″	11.7	19.5	969	2.7
OM15K-6W	Khafifah	58°25′27.29″	22°54′16.55″	10.7	20	718	2.9
OM15K-8W	Khafifah	58°25′27.25″	22°54′16.25″	9.8	22.9	666	3.5
OM15K-10W	Khafifah	58°25′27.46″	22°54′16.34″	10.4	23.5	713	2.6
OM15K-13W	Khafifah	58°25′27.74″	22°54′16.00″	11.2	22.2	790	3.0
OM15K-16W	Khafifah	58°25′28.56″	22°54′15.83″	11.6	23.5	954	2.5
OM15K-18W	Khafifah	58°25′29.09″	22°54′15.47″	11.5	23.6	912	2.5
OM15K-19W	Khafifah	58°25′29.21″	22°54′15.19″	10.4	23.9	1039	2.3
OM15K-20W	Khafifah	58°25′29.95″	22°54′15.19″	11.5	24	927	npm[a]
OM15K-21W	Khafifah	58°25′30.67″	22°54′14.33″	11.5	22.5	927	npm
OM15K-22W	Khafifah	58°25′30.87″	22°54′14.23″	11.1	23.3	818	1.9

[a] Not possible to measure.

spectroscopy using a Varian Vista Pro ICP-OES device. Sulfate (SO_4^{2-}) and chloride (Cl^-) concentrations in alkaline water samples were determined using a Metrohm 882 Compact IC Plus ion chromatograph (IC). Analytical accuracy obtained from the measurement of certified reference materials (TMDW-A, IAPSO seawater) was better than 0.25% for IC analyses and better than 8% (Ca, K, Mg, Si, Ba, Sr) and 13.8% (Na) for ICP-OES measurements. Further element analyses on 10-fold diluted water samples were conducted using a double-focusing magnetic sector field inductively coupled plasma mass spectrometer (Thermo Finnigan Element2™, Germany).

The mineralogy of the samples was determined by powder X-ray diffraction (XRD), using a PANalytical MPD diffractometer with a Bragg-Brentano parafocusing geometry and Cu K_a radiation (operating at 40 mA and 45 kV). Instrument configuration included programmable divergence slits in the incident and diffracted beams, placement of a 0.25° fix anti-scatter slit in the incident path and a PSD detector PIXel. Data processing was conducted by using the software HighScore Plus from PANalytical X'Pert PRO (mineral database: Pdf2HSP/PAN-ICSD). Mineral quantification was defined by the peak refining method described in Rietveld (1969). Recently formed precipitates collected from the spring sites were analyzed both wet and dried in order to detect hydrated, labile phases that might be present within the pools. The textural characterization and semi-quantitative chemical analysis of the solid samples were carried out at the Centro de Instrumentacion Científica (CIC) of the University of Granada (Granada, Spain) using a Field Emission Scanning Electron Microscope (FE-SEM) ZEISS AURIGA (In-Lens mode at 3 kV) and an Environmental SEM (ESEM) FEI Quanta 400 (SE mode at 5 kV and BSE mode at 12 kV). Complementary analysis of mineral phases and textures was carried out at CIC using a FE-SEM Zeiss Supra 40Vp conneted to a Renishaw In Via Raman spectrometer fitted with a Nd:YAG 532 nm laser and a near infrared diode 785 nm laser, with maximum powers of 500 mW and 100 mW, respectively. The SEMs were equipped with Energy Dispersive X-ray Spectrometers (EDS).

4. Results

4.1. Chemical composition of alkaline waters

The physicochemical parameters and chemical composition of the collected water samples are presented in Tables 1 and 2, respectively. We subdivided the waters into three types according to their chemical and hydrological characteristics: i) Mg-type; moderately alkaline ($7.9 < pH < 9.5$), Mg^{2+}–HCO_3^--rich waters, ii) Ca-type; hyperalkaline ($pH > 11.6$), Ca^{2+}–OH^--rich waters, and iii) Mix-type; alkaline to hyperalkaline ($9.6 < pH < 11.5$) waters with intermediate chemical composition. In the present study, we use the terms “Mg-type” instead of Mg^{2+}–HCO_3^--rich waters (Type I) and “Ca-type” instead of Ca^{2+}–OH^--rich waters (Type II). We also use the term “Mix-type” to refer to all the waters formed by the mixing of Mg-type and Ca-type waters (Fig. 1).

The two studied spring sites are small-scale, hydrological networks of pools formed upon the discharge of Ca-type and Mg-type waters (Fig. 4A). Mg-type waters occur in spring and run-off waters forming pools with diameters from 0.5 to 2 m, and emanate from rock fractures usually associated with soils (Fig. 4B). They have high Mg (1.4 to 7.2 mmol L^{-1}) and DIC (4 to 14.6 mmol L^{-1}) concentration, and relatively low Ca concentration (0.2 to 0.4 mmol L^{-1}). Ca-type waters

Table 2
Major ion and trace element chemistry of water samples.

Sample ID	Ba (μmol L^{-1})	Ca (mmol L^{-1})	K (mmol L^{-1})	Mg (mmol L^{-1})	Na (mmol L^{-1})	Si (mmol L^{-1})	Sr (μmol L^{-1})	Cl^- (mmol L^{-1})	SO_4^{2-} (mmol L^{-1})	DIC (mmol L^{-1})
Mg-type										
OM15-1W	0.044	0.382	0.029	2.497	0.869	0.391	2.705	0.982	0.378	4.713
OM15-2W	0.044	0.317	0.029	2.430	1.003	0.297	2.648	1.222	0.478	4.040
OM15K-2W	0.604	0.183	0.279	7.167	16.921	0.112	0.262	16.623	0.649	14.66
OM15K-7W	0.692	0.425	0.021	2.837	1.110	0.335	2.762	1.424	0.358	5.810
OM15K-23W	0.801	0.249	0.051	1.373	1.618	0.145	1.016	1.657	0.292	2.521
Ca-type										
OM15-4W	0.029	1.793	0.127	0.002	5.228	0.006	1.335	5.121	0.002	0.993
OM15-9W	0.029	1.603	0.118	0.017	4.850	0.006	1.278	4.814	0.006	1.006
OM15K-1W	2.709	1.954	0.162	0.003	6.055	0.006	1.586	5.176	0.007	1.319
OM15K-3W	1.260	1.666	0.149	0.005	6.255	0.005	1.472	5.364	0.008	1.329
OM15K-4W	2.381	1.703	0.140	0.010	6.072	0.009	1.507	5.190	0.008	1.422
OM15K-9W	1.995	2.035	0.143	0.001	6.277	0.003	1.404	5.244	0.005	0.379
OM15K-11W	0.990	1.944	0.150	0.002	7.151	0.003	1.405	5.941	0.005	1.661
OM15K-14W	1.405	2.043	0.154	0.003	6.886	0.024	1.518	5.503	0.005	1.705
Mix-type										
OM15-3W	bdl[a]	0.141	0.095	0.578	3.992	0.112	0.137	4.028	0.120	0.709
OM15-5W	0.029	0.460	0.041	2.019	1.619	0.256	2.305	1.804	0.407	3.655
OM15-6W	0.022	0.431	0.047	1.891	1.892	0.238	1.666	2.056	0.379	3.765
OM15-8W	bdl	0.147	0.073	1.176	3.058	0.151	0.183	3.095	0.231	1.565
OM15-11W	0.007	0.188	0.080	1.066	3.354	0.137	0.205	3.254	0.212	1.329
OM15-12W	0.015	0.152	0.079	1.043	3.336	0.123	0.171	3.311	0.214	1.451
OM15K-5W	0.801	0.611	0.120	0.373	5.194	0.043	0.856	4.671	0.063	1.168
OM15K-6W	0.626	0.339	0.104	0.749	4.589	0.088	0.787	4.163	0.126	2.016
OM15K-8W	0.670	0.292	0.078	1.384	3.678	0.162	1.187	3.365	0.207	3.183
OM15K-10W	0.837	0.357	0.097	0.901	4.347	0.115	0.536	3.898	0.144	1.773
OM15K-13W	0.881	0.177	0.099	1.016	4.301	0.109	0.194	3.770	0.176	1.912
OM15K-16W	0.786	0.499	0.121	0.220	5.459	0.055	0.377	4.520	0.099	1.018
OM15K-18W	0.619	0.459	0.122	0.162	5.529	0.052	0.331	4.588	0.093	1.011
OM15K-19W	0.910	0.124	0.203	0.019	8.686	0.044	0.662	7.575	0.012	1.756
OM15K-20W	1.966	0.446	0.124	0.140	5.694	0.050	0.377	4.673	0.086	npm[b]
OM15K-21W	2.287	0.351	0.127	0.069	5.890	0.039	0.285	4.807	0.076	npm
OM15K-22W	0.721	0.150	0.130	0.076	6.029	0.035	0.126	4.873	0.081	0.999

[a] Below detection limit.
[b] Not possible to measure.

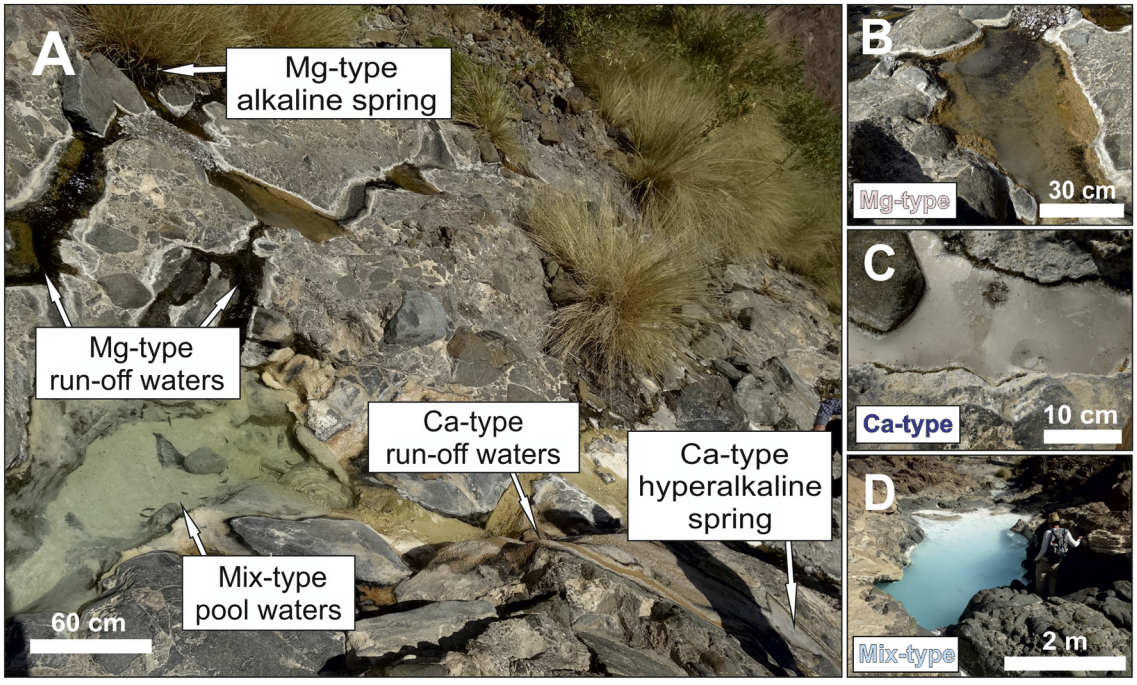

Fig. 4. Hydrological network and water types in the Nasif site, forming upon the discharge of circulating waters in the peridotites. A: Overview photograph showing the type of springs, pools and run-off waters in the Nasif spring site. Upstream to downstream direction is from top-right to bottom-left. B: Mg-type waters mantled by white rock coatings. C: Ca-type waters hosting a crystalline crust floating on their surface. D: Mix-type waters; often demonstrating turquoise colored waters. (For interpretation of the references to color in this figure legend, the reader is referred to the web version of this article.)

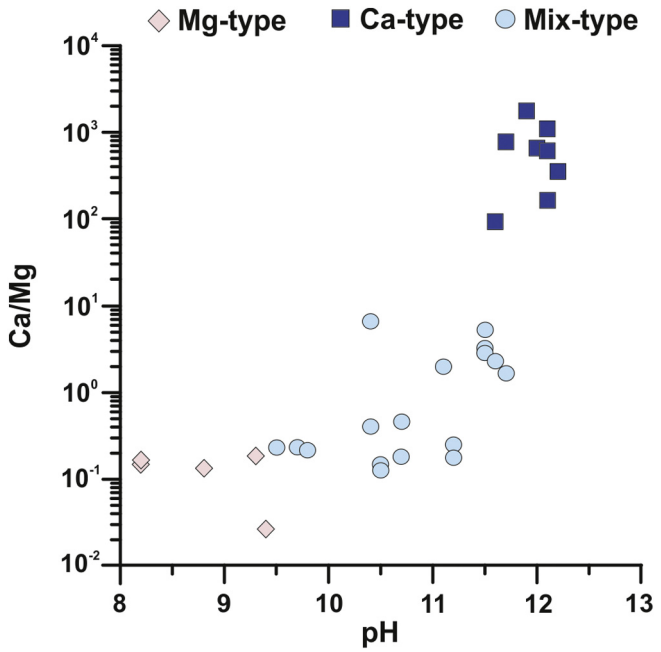

Fig. 5. Graph showing the relationship of Ca/Mg ratio with the pH in the different water types. Mg-type waters are mildly alkaline and show low Ca/Mg ratios. Ca-type waters are hyperalkaline and show high Ca/Mg ratios. Mix-type waters demonstrate a wide range in pH values and intermediate Ca/Mg ratios.

include shallow pools (in most cases up to 0.5 m in diameter) with a thin crystalline crust floating on the water surface (Fig. 4C). They show high Ca concentration (up to 2 mmol L^{-1}), low DIC (0.4 to 1.7 mmol L^{-1}), and virtually no Mg (0.001 to 0.02 mmol L^{-1}). Ca-type waters form isolated pools discharging from either tectonic fractures or small cracks and fissures in the ultramafic rocks. The hydrological network of the pools develops through mixing of the run-off waters of the two different spring water types (Figs. 1; 4A). Pools of Mix-type waters—that are predominant in the two spring sites—show great variability in diameter (0.5–7 m) and habitually display a turquoise color (Fig. 4D). Mix-type waters have variable Ca (0.1–0.6 mmol L^{-1}) and Mg (0.02–2 mmol L^{-1}) concentrations, intermediate between Mg-type and Ca-type waters, and DIC values between 0.7 and 3.8 mmol L^{-1}. The graph in Fig. 5 highlights the categorization of the three different water types, based on the relationship of Ca/Mg ratio with the pH.

4.2. Mineralogy and textures

The mineralogy of the different types of solid samples and their chemical formulas in the studied spring sites are given in Tables 3 and 4, respectively. We have identified four mineral groups: anhydrous carbonates (calcite, aragonite, and dolomite), hydroxides (brucite), layered double hydroxides (LDH; hydrotalcite) and, hydrated (hydroxy-) carbonates (nesquehonite, dypingite, hydromagnesite and artinite). Olivine and serpentine group minerals—identified in a fraction of the samples—are most likely detritus from the ultramafic host rocks, and quartz probably derives from wind-blown dust from the nearby Wahiba Sands desert (40 km SE from the spring sites). Table 5 summarizes the percentage of the identified mineral phases to the total mineralogical index in each sample type for both sites, and Table 6, presents the wt% range in mineral composition for each type of solid samples. All samples contain calcium carbonate phases, and brucite is present in 22% of them. Hydrated magnesium (hydroxy-) carbonates, LDH phases, and dolomite are found in 7%, 2% and 2% of the total number of collected samples, respectively.

4.2.1. Crystalline crusts

We identified two types of crystalline crusts in the spring sites: i) calcitic crusts (90–100 wt%; Table 6) in Ca-type waters, and ii) aragonite-dominated crusts (60–72 wt%) in Mix-type waters. Calcitic crusts in Ca-type waters are thin (< 1 mm) and form on the air-water interface. They are rather homogeneous and almost exclusively composed of aggregates of subhedral {120} calcite crystals (up to 40 μm), growing laterally to the air-water interface towards the water column (Fig. 6A). Patches of subhedral to anhedral calcite crystals (< 4 μm) can be also observed in between the main subhedral calcite crystals (Fig. 6A).

Crystalline crusts in Mix-type waters are rare and occur where Mg-type and Ca-type spring water outlets discharge in the same pool. They typically form near the outlet of Ca-type waters, and their growth is restricted towards the central parts of the pool. Unlike Ca-type water crusts, the mineralogy in Mix-type water crusts is heterogeneous and is composed of aragonite (50–75 wt%), brucite (10–35 wt%), calcite (4–12 wt%), and sometimes hydromagnesite (0–15 wt%) (Fig. 6C, D). Aragonite exhibits acicular, needle-like morphologies, with needle-like crystal sizes ranging from < 1 to 20 μm. In the aragonite-dominated crusts, dispersed euhedral to subhedral (5 to 30 μm) calcite crystals grow on the aragonitic crust surface (Fig. 6C). Brucite occurs as single spheres (avg. diameter of 40 μm) made of interlocking flakes (Fig. 6C), and hydromagnesite as rosette clusters with flower-like morphologies of variably spaced flaky crystals (Fig. 6D).

4.2.2. Rock coatings

The rock coating materials mantle some Mg-type and Ca-type pools just above the water surface. The mineralogy of rock coatings in Mg-type waters is diverse and includes calcium carbonate phases (0–15 wt % calcite and aragonite), hydrated magnesium carbonates (5–70 wt% nesquehonite, 0–25 wt% dypingite, 0–12 wt% hydromagnesite and 0–5 wt% artinite), and halite (0–20 wt%) (Fig. 7). Aragonite occurs as individual, spindle crystals (< 15 μm; Fig. 7A), and calcite as subhedral crystal clusters (< 40 μm; Fig. 7B). Nesquehonite exhibits variably sized, prismatic crystals (40–2000 μm; Fig. 7B, C) and dypingite and hydromagnesite show rosettes (< 40 μm) made of flaky crystals (Fig. 7C). Halite—formed during evaporation at the edges of the pools—appears as integrating {111} octahedral crystals (Fig. 7A) or crusts on the surfaces of other minerals (Fig. 7C).

Rock coatings in Ca-type waters are made of calcite (70–90 wt%) and aragonite (10–30 wt%) showing subhedral to euhedral crystals (Fig. 7D). Integrating, euhedral {104} calcite crystals (up to 50 μm) coexist with {120} curved edged calcite (up to 120 μm), which exhibits step growth (Fig. 7D). Where present, aragonite shows acicular morphologies of tubular crystals ranging in size from 5 to 80 μm (Fig. 7D).

4.2.3. Flocculent material

The flocculent material consists of particles in suspension within the water column that eventually form unconsolidated deposits at the bottom of the pools. They mostly occur in the Mix-type waters; we have only found one sample of this sample type in Ca-type waters at the Khafifah site (sample OM15K-01A-P; Table 3). Aragonite (5–25 μm) is the main component of the flocculent particles (75–100 wt%) and exhibits diverse textures including initial crystalline sheaves, dumbbell, wheat-sheaf, and acicular-spheroidal morphologies (Fig. 8A). Brucite crystals, with low degree of crystallinity, and flakes of LDH phases are occasionally attached to aragonite particles (Fig. 8B).

4.2.4. Mud-like precipitates

Mud-like precipitates are white to yellow/brown material only occurring in Mix-type waters. They mainly form at shallow parts of the pool network, such as the pool and stream edges, or shallow areas of Mix-water pools. Occasionally, mud-like precipitates form dams (rippled terracing) in pools and streams associated with active water flow.

Table 3
Mineralogy of solid sample types collected from the spring sites.

Sample	Site	Water type	Sample type description	Mineralogy	
				Major	Minor
OM15-02B-R	Nasif	Mg-type	Rock coatings	Calcite	Aragonite, halite, nesquehonite
OM15-03A-P	Nasif	Mix-type	Crystalline crust	Aragonite	Brucite, calcite, hydromagnesite
OM15-03B-P	Nasif	Mix-type	Crystalline crust	Aragonite, brucite	Calcite
OM15-03C-Pa	Nasif	Mix-type	Mud-like (pool)	Aragonite, brucite	Calcite
OM15-03C-Pb	Nasif	Mix-type	Mud-like (pool)	Aragonite	Calcite
OM15-03D-P	Nasif	Mix-type	Mud-like (pool)	Aragonite	–
OM15-03E-P	Nasif	Mix-type	Flocculent material (pool)	Aragonite, calcite, brucite	Quartz, hydromagnesite
OM15-04A-P	Nasif	Ca-type	Crystalline crust	Calcite	Aragonite
OM15-04B-R	Nasif	Ca-type	Rock coatings	Calcite	Aragonite
OM15-05F-P	Nasif	Mix-type	Mud-like (stream)	Aragonite	Calcite
OM15-05G-P	Nasif	Ca-type	Lithified structures (dam-like)	Calcite	Aragonite
OM15-05H-P	Nasif	Mix-type	Lithified structures (concretions)	Aragonite, brucite	Calcite
OM15-06A-P	Nasif	Mix-type	Mud-like (stream)	Calcite, aragonite	–
OM15-06B-P	Nasif	Mix-type	Mud-like (stream)	Aragonite	–
OM15-08A-P	Nasif	Mix-type	Mud-like (pool)	Aragonite	–
OM15-08B-P	Nasif	Mix-type	Flocculent material (pool)	Aragonite	–
OM15-08C-P	Nasif	Mix-type	Mud-like/dam (stream)	Aragonite	–
OM15-08D-P	Nasif	Mix-type	Mud-like/dam (stream)	Aragonite	–
OM15-08E-P	Nasif	Mix-type	Mud-like/dam (stream)	Aragonite	–
OM15-08F-P	Nasif	Mix-type	Flocculent material (stream)	Aragonite, brucite	Calcite
OM15-08G-P	Nasif	Mix-type	Mud-like/dam (stream)	Aragonite	–
OM15-08H-P	Nasif	Mix-type	Mud-like/dam (stream)	Aragonite	–
OM15-08I-P	Nasif	Mix-type	Mud-like/dam (stream)	Aragonite	–
OM15-09A-P	Nasif	Ca-type	Mud-like (pool)	Aragonite, calcite, brucite	–
OM15-10A-P	Nasif	Mix-type	Mud-like/dam (stream)	Aragonite	–
OM15-10B-Pa	Nasif	Mix-type	Mud-like (pool)	Aragonite	Calcite
OM15-10B-Pb	Nasif	Mix-type	Mud-like (pool)	Aragonite	–
OM15-10D-Ra	Nasif	–	Travertine terrace	Mg-calcite, aragonite	–
OM15-10D-Rb	Nasif	–	Travertine terrace	Calcite, dolomite	Aragonite, chrysotile
OM15-10E-P	Nasif	Mix-type	Mud-like/dam (stream)	Aragonite	–
OM15-12B-Pa	Nasif	Mix-type	Mud-like (pool)	Aragonite	Calcite
OM15-12B-Pb	Nasif	Mix-type	Mud-like (pool)	Aragonite	–
OM15K-01A-P	Khafifah	Ca-type	Flocculent material (pool)	Aragonite, calcite	Brucite
OM15K-01B-P	Khafifah	Ca-type	Crystalline crust	Aragonite, calcite	–
OM15K-02A-R	Khafifah	Mg-type	Rock coatings	Nesquehonite, dypingite, hydromagnesite	Calcite, aragonite, halite, (Cl-)artinite
OM15K-02B-R	Khafifah	Mg-type	Rock coatings	Nesquehonite, dypingite, hydromagnesite	Halite, calcite, aragonite, artinite, quartz
OM15K-03A-P	Khafifah	Mix-type	Mud-like/dam (stream)	Aragonite, calcite	Quartz
OM15K-05B-P	Khafifah	Mix-type	Mud-like/dam (stream)	Aragonite, calcite	Brucite
OM15K-05B-P	Khafifah	Mix-type	Flocculent material (pool)	Aragonite	Brucite, calcite, LDH (hydrotalcite)
OM15K-07A-R	Khafifah	Mg-type	Rock coatings	Nesquehonite	Dypingite, hydromagnesite, halite, aragonite, quartz
OM15K-09A-P	Khafifah	Mix-type	Mud-like (pool)	Calcite	Aragonite
OM15K-10A-P	Khafifah	Mix-type	Mud-like (pool)	Aragonite, calcite	–
OM15K-10C-P	Khafifah	Mix-type	Mud-like (pool)	Aragonite, calcite	–
OM15K-12A-P	Khafifah	Mix-type	Mud-like (pool)	Aragonite, calcite	–
OM15K-12B-P	Khafifah	Mix-type	Flocculent material (pool)	Aragonite	Calcite
OM15K-13C-P	Khafifah	Mix-type	Flocculent material (pool)	Aragonite, calcite	Brucite
OM15K-13D-P	Khafifah	Mix-type	Flocculent material (pool)	Aragonite	–
OM15K-13E-Pa	Khafifah	Mix-type	Mud-like (pool)	Aragonite, halite	–
OM15K-13E-Pb	Khafifah	Mix-type	Mud-like (pool)	Aragonite, halite	–
OM15K-14A-P	Khafifah	Ca-type	Crystalline crust	Calcite	–
OM15K-14A-P	Khafifah	Ca-type	Crystalline crust	Calcite	–
OM15K-14B-Pa	Khafifah	Ca-type	Crystalline crust	Calcite	Aragonite
OM15K-14-R	Khafifah	–	Travertine terrace	Calcite	Aragonite, chrysotile, Fe-oxides, Cr-spinel
OM15K-15A-P	Khafifah	Mix-type	Mud-like/dam (stream)	Aragonite	–
OM15K-17A-P	Khafifah	Mix-type	Mud-like/dam (stream)	Aragonite, brucite	–

Table 4
Chemical formulas of mineral phases identified in the spring sites.

Mineral	Chemical formula
Calcite, aragonite	$CaCO_3$
Dolomite	$CaMg(CO_3)_2$
Brucite	$Mg(OH)_2$
Hydrotalcite	$Mg_6Al_2(OH)_{16}(CO_3)\cdot 4H_2O$
Nesquehonite	$MgCO_3\cdot 3H_2O$
Dypingite	$Mg_5(CO_3)_4(OH)_2\cdot 5H_2O$
Hydromagnesite	$Mg_5(CO_3)_4(OH)_2\cdot 4H_2O$
Artinite	$Mg_2(CO_3)(OH)_2\cdot 3H_2O$

Aragonite is the predominant mineral phase (63–100 wt%) in mud-like precipitates, displaying a homogeneity in morphological and textural features (crystal sizes range from < 1 μm to 15 μm) (Fig. 9A). The most common aragonite morphologies are spindle (c. 80 vol%; Fig. 9B) followed by spheroidal aragonite clusters made of small (< 3 μm) needle-like crystals (Fig. 9B). Calcite (0–37 wt%; 2–5 μm in size) and brucite (0–16 wt%; < 500 nm in size) are commonly associated with needle-like aragonite (Fig. 9C). In some cases, aragonite shows penetration twinning with crystal sizes varying from < 1 μm to 10 μm (Fig. 9D).

4.2.5. Lithified structures

Samples of lithified structures include dam-like formations, concretions associated with active water flow, and travertine terraces on

Table 5
Percentages of the mineral phases to the total mineralogical index in each solid sample type.

Solid sample type	Site	$CaCO_3$ (calcite/ aragonite)	Dolomite	Brucite	Hydrated Mg-carbonates	LDHs
Crystalline crusts	Nasif	100%	0%	66.6%	33.3%	0%
	Khafifah	100%	0%	0%	0%	0%
Rock coatings	Nasif	100%	0%	0%	50%	0%
	Khafifah	100%	0%	0%	100%	0%
Flocculent material	Nasif	100%	0%	66.6%	33.3%	0%
	Khafifah	100%	0%	60%	0%	20%
Mud-like precipitates	Nasif	100%	0%	10%	0%	0%
	Khafifah	100%	0%	20%	0%	0%
Lithified structures	Nasif	100%	25%	25%	0%	0%
	Khafifah	100%	0%	0%	0%	0%

ultramafic rocks that are presently unrelated to active water flow. Dam-like formations are whitish, yellowish or reddish, and they are commonly associated with microbial mats. Calcite is the dominant phase of the dam-like formations (85–100 wt%) and exhibits an internal layering that terminates into curved and sharp edges on the exterior part (Fig. 10A). Small amounts of needle-like aragonite (0–15 wt%) can be observed at the external parts of the dams (Fig. 10A).

The concretions consist of aragonite (55 wt%), brucite (36 wt%), and calcite (9 wt%), and they are locally observed in restricted zones, where run-off Ca-type waters mix with Mg-type or Mix-type waters. Aragonite occupies the lower part of the concretions (in contact with the ultramafic bedrock) and shows a massif cementation texture that becomes needle-like (< 5 μm) at the exterior part (facing the water column). Brucite displays a compact texture with narrow spaces between the flaky crystals that compose the brucite clusters (Fig. 10B).

Calcite is the main component (76–90 wt%) of travertine samples, whilst aragonite (5–14 wt%) and dolomite (0–8 wt%) are present as minor phases. Traverine samples display recrystallization textures with variable crystal sizes (< 1 μm to > 200 μm), different generations of vein networks, and chaotic and colloformic textural features (Fig. 10C). Clasts of serpentinite, Fe-oxides, and Cr-spinel from the ultramafic host rocks occasionally occur in the carbonate matrix of the travertine (Fig. 10D).

4.3. Thermodynamic models

4.3.1. Mineral saturation indices

The mineral saturation indices (SIs) in the investigated water samples (Fig. S2 Supplementary Material) were calculated using the geochemical speciation and reaction path modeling code PHREEQC (Parkhurst and Appelo, 1999) and the wateq4f database. Fig. 11 shows the SI of potential mineral phases as a function of the partial pressure of CO_2 (P_{CO2}) in the three water types from the Nasif and Khafifah spring sites. Calcium carbonate (calcite + aragonite) has the highest SI values in Ca-type waters (avg. SI = 1.95) and systematically decreases in Mix-type waters (avg. SI = 1.33) and Mg-type waters (avg. SI = 0.85) that show the lowest SI values. Mg-type waters and Mix-type waters with pH < 10.5 are undersaturated with respect to brucite (avg. SI = −2), whereas brucite is supersaturated in Ca-type waters and Mix-type waters with pH > 10.5 (avg. SI = 1). All water types are undersaturated with respect to nesquehonite that is close to saturation in Mg-type waters. Ca-type and Mg-type waters are undersaturated with respect to artinite and hydromagnesite. The SIs of these minerals increase in Mix-type waters where hydromagnesite is supersaturated in some samples, and artinite is supersaturated (avg. SI = 1.2) in most samples. Quartz SIs are positively correlated with P_{CO2} that corresponds to a transition from quartz-undersaturated Ca-type waters to quartz-saturated Mg-type waters. Most Khafifah waters show lower P_{CO2} values than Nasif waters, indicating that Khafifah waters are less equilibrated with the atmosphere.

4.3.2. Mixing model

The spatial distribution and the undisturbed nature of the pools in the Nasif site allow to accurately compare the water chemical compositions derived by analytical techniques to those acquired by mixing model calculations. The positive correlation (r^2 = 0.9992) of the conservative tracers Cl^- and Na points that the physicochemical variability of the Nasif site waters is due to variable mixing of two water end-members with the highest and lowest Cl^- and Na concentrations, respectively. To evaluate the role of water mixing in mineral precipitation, we performed mixing model calculations using the PHREEQC-MIX command. For modeling, we use as end-members pristine Ca-type (OM15-1W) and Mg-type spring water samples (OM15-4W) with the highest and lowest Cl^- and Na concentrations (Table 2), respectively. The modeling was computed to mix the Mg-type water end-member with the Ca-type end-member under a mixing ratio step of 0.01 (1%) (Fig. 12). This permits to follow and examine the SI of the minerals under all the intermediate mixing ratios between the two pristine end-members (100% = 1; Fig. 12) of Mg-type and Ca-type waters.

Fig. 12 models the evolution of the SIs of selected mineral phases, $CO_{2(g)}$ and pH with increasing mixing fraction—from left to right—of the Ca-type water end-member. Calcite and aragonite are supersaturated for all mixing fractions and their SIs reach a plateau, where Ca-type water mixing fraction is between 0.3 and 1 (Fig. 12). Brucite becomes saturated at Ca-type water mixing fraction > 0.25, where pH is > 9.8. Brucite SI value continues to increase (c. 2.5) up to 0.95 Ca-type water mixing fraction, where it rapidly decreases (Fig. 12). Artinite reaches saturation at 0.12 Ca-type water mixing fraction, and its SI value increases up to Ca-type fraction of 0.6, where the pH value is 11.2 (Fig. 12). Similar to brucite, artinite presents an extreme SI value decrease between 0.95 and 1 Ca-type water mixing fraction that leads to its undersaturation. Hydromagnesite—which SI values display a bell-shaped curve—is supersaturated between 0.15 and 0.8 Ca-type water

Table 6
Compositional range of mineral phases by solid sample type found in the different water types.[a]

Solid sample type	Water type	Calcite	Aragonite	Dolomite	Brucite	Nesquehonite	Dypingite	Hydromagnesite	Artinite	LDH
Crystalline crusts	Ca-type	90–100	0–10	–	–	–	–	–	–	–
	Mix-type	5–15	50–70	–	10–35	–	–	0–10	–	–
Rock coatings	Mg-type	0–15	0–5	–	–	5–70	0–25	0–15	0–5	–
	Ca-type	70–90	10–30	–	–	–	–	–	–	–
Flocculent material	Ca-type	10	74	–	12	–	–	–	–	4
	Mix-type	0–15	75–100	–	0–15	–	–	–	–	–
Mud-like precipitates	Mix-type	0–37	63–100	–	0–16	–	–	–	–	–
Lithified structures:										
i) Travertine terraces	–	76–90	5–14	0–8	–	–	–	–	–	–
ii) Dam-like formations	Ca-type	85–100	0–15	–	–	–	–	–	–	–
iii) Concretions	Mix-type	9	55	–	36	–	–	–	–	–

[a] Values in wt%

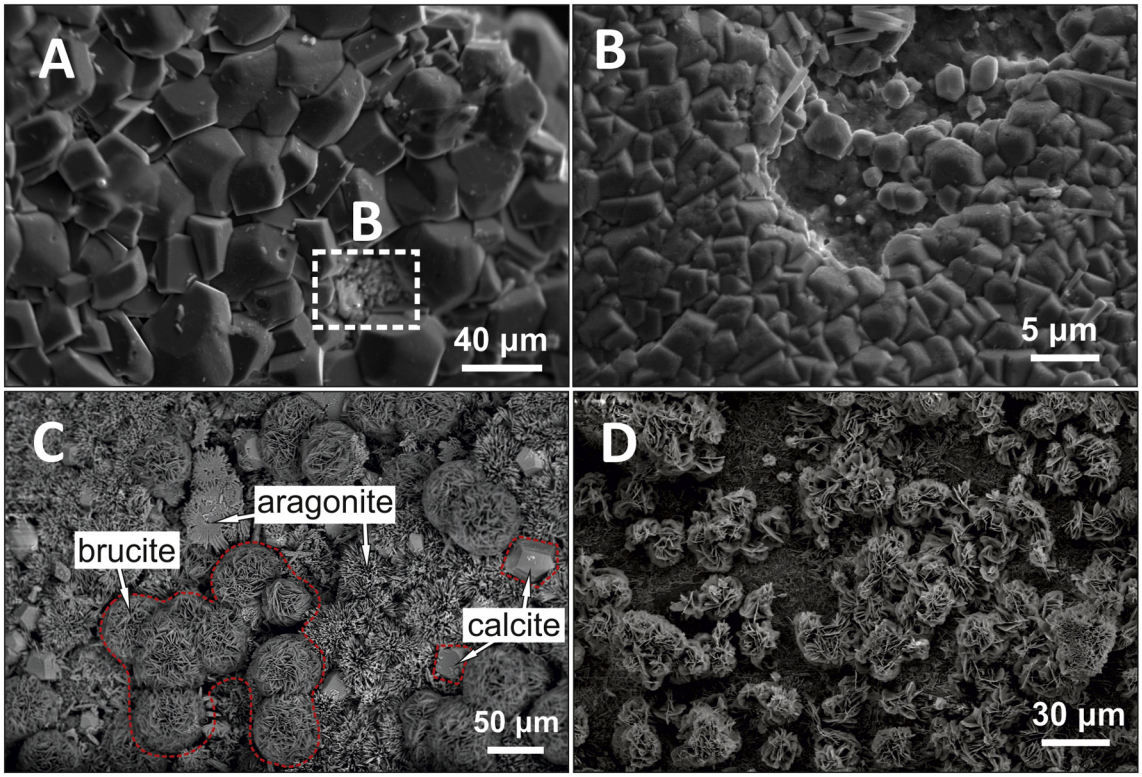

Fig. 6. SEM images of crystalline crusts precipitating on the surface of Ca-type and Mix-type waters. A: Calcite-dominated crystalline crust in Ca-type waters. B: Zoomed-in image of the calcite crystals from the inset in A, showing patches of subhedral to anhedral calcite crystals in between larger calcite crystals. C: Aragonite, brucite and calcite assemblage in a crystalline crust in Mix-type waters. D: Hydromagnesite and brucite clusters grow on an aragonitic crust in Mix-type waters.

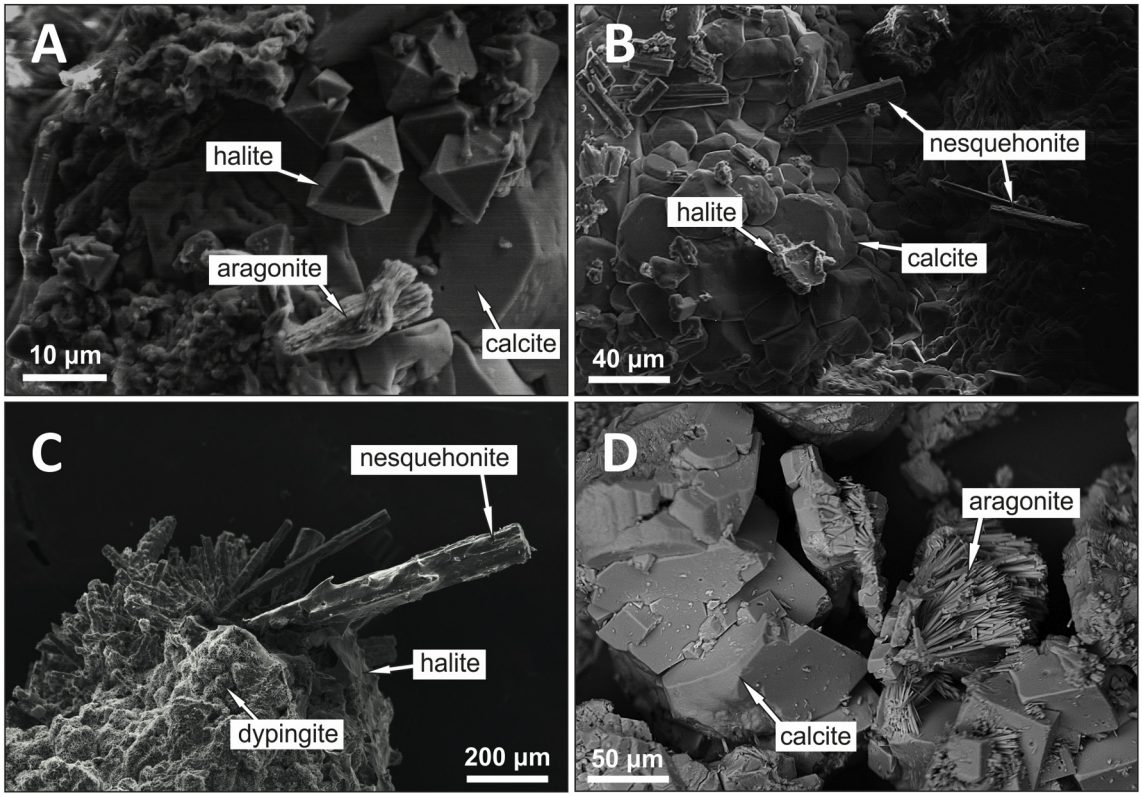

Fig. 7. SEM images of rock coatings precipitating around the pools. A: Mineral assemblage of calcite, octahedral halite and spindle-like aragonite in Mg-type waters of the Nasif site. B: Prismatic nesquehonite, calcite with curved edges and halite in Mg-type waters of the Nasif site. C: Large prismatic crystals of nesquehonite grow on rosette-like aggregates of dypingite in Mg-type waters. D: Acicular aragonite crystals and calcite with curved edges associated with Ca-type waters.

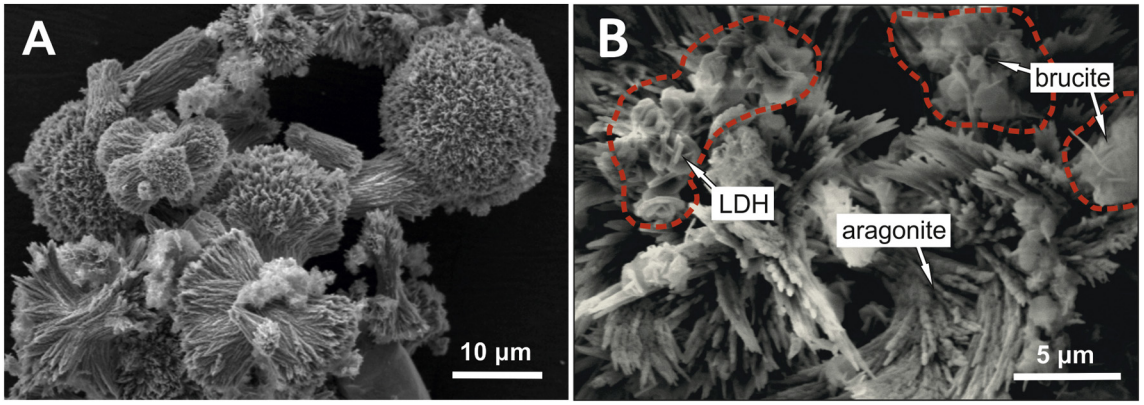

Fig. 8. SEM images of flocculent material depositing at the bottom of the pools or being in suspension within the water column. A: Textural variability of aragonite including initial crystalline sheaves, dumbbell, wheat-sheaf, and acicular-spheroidal morphologies in Mix-type waters. B: Brucite and LDH (hydrotalcite) crystals found attached on aragonite crystals in Mix-type waters.

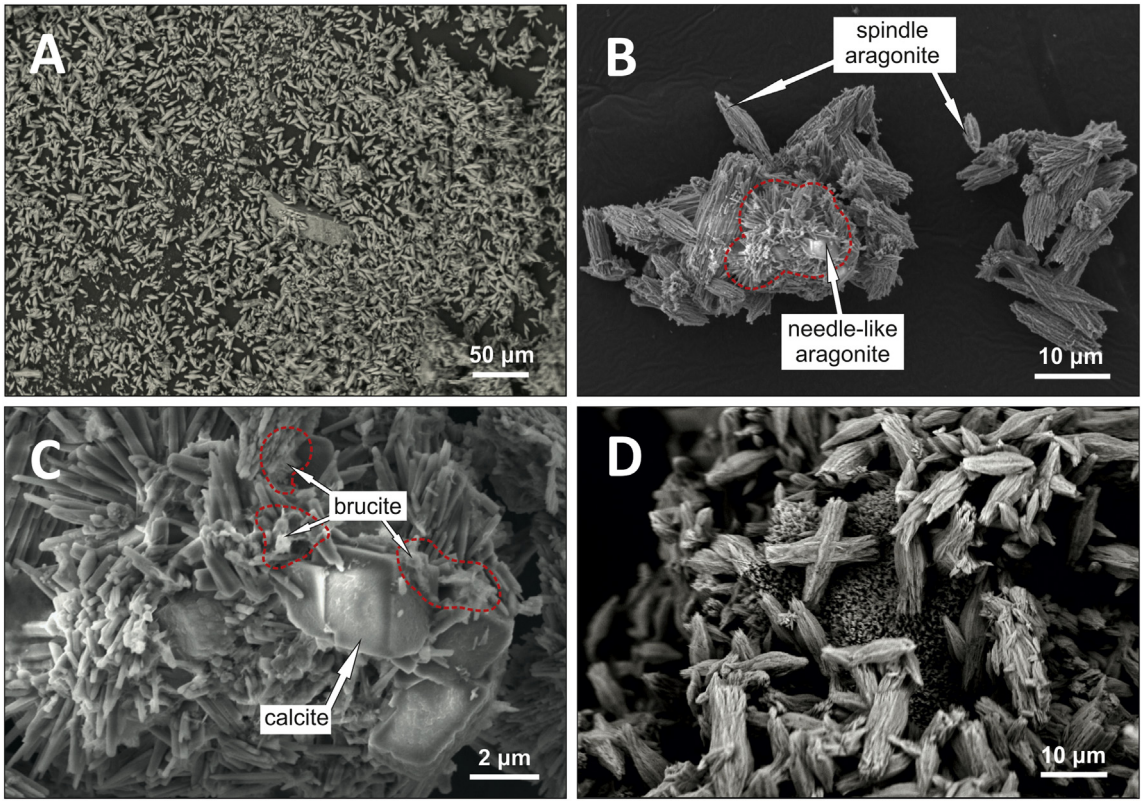

Fig. 9. SEM images of mud-like precipitates forming inside and around the pools. A: Overview of aragonite-dominated mud-like precipitates. B: Spindle and needle-like morphologies of aragonite crystals and crystal aggregates in mud-like precipitates. C: Needle-like clusters of aragonite along with calcite and brucite crystals. D: Aragonite crystals exhibiting (cruciform) penetration twinning sit on spheroidal needle-like aragonite.

mixing fraction (Fig. 12). Nesquehonite is undersaturated for all mixing fractions; its SI increases in the 0–0.15 Ca-type water fraction interval, while it decreases with increasing Ca-type water mixing fraction (from 0.4 to 1)(Fig. 12).

The same water samples used as end-members for the mixing model in Fig. 12 were also used to calculate the theoretical mixing proportion of Mg-type and Ca-type water type in each collected water sample from the Nasif spring site (Fig. 13). Measured (analytical) versus estimated (PHREEQC) values of element concentrations (Fig. 13) in the Nasif water samples are well correlated ($R^2 > 0.95$) for K, Na, Cl^-, and Mg, whereas Ca, Al, Si, Sr, Ba, SO_4^{2-} and DIC show a larger dispersion and correlation. Estimated values of Ba, Sr, Ca, K, Si, Al, DIC are higher than the measured ones in the majority of the samples, whereas SO_4^{2-} shows higher measured values.

5. Discussion

5.1. Groundwater flow paths of Oman alkaline springs

In the Oman spring systems, the proximity of the outlets of Mg-type and Ca-type water springs—somewhere spaced close together c. 1 m—(Fig. 4A) raises the question of what are the underground flow paths of these two types of water. In the Oman Ophiolite, groundwater circulation occurs in the near-surface horizon of fissured serpentinized peridotite, and to a lesser extent, along deeper fractures (Dewandel et al., 2003). Although tectonic structures (e.g., faults) might act as

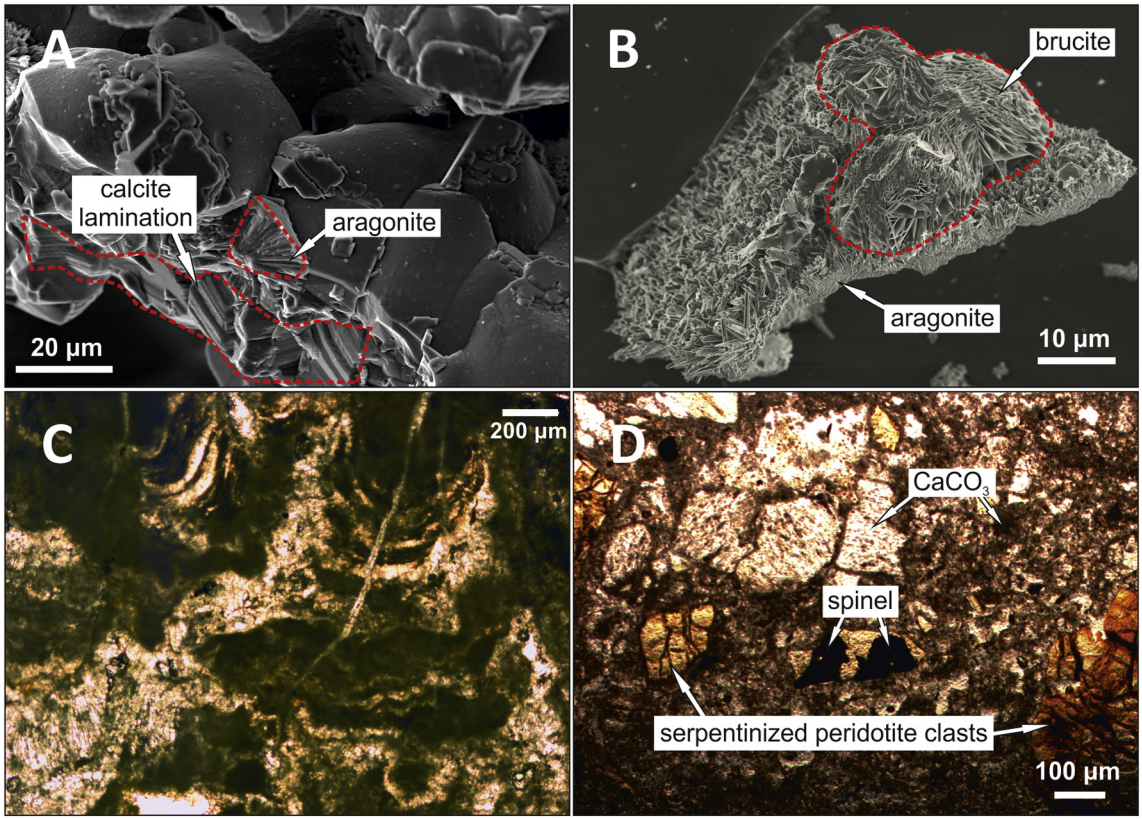

Fig. 10. SEM and optical microscope images of lithified structures associated with Ca-type and Mix-type waters or collected from travertine terraces. A: SEM image of calcite-dominated dam-like structures associated with active flow of Ca-type waters. The dams exhibit an internal layering that terminates into a curved and smoothened exterior part. Needle-like aragonite occurs at the external part of the dam. B: SEM image of concretions containing brucite clusters that grow on a substrate of acicular aragonite. This type of sample occurs at the mixing zones of Ca-type and Mix-type waters. C: Optical microphotograph of travertine thin section exhibiting colloformic and chaotic textures of calcium carbonate (transmitted light). D: Optical microphotograph of travertine thin section composed of clasts from the serpentinized host rocks that are entrapped in the calcium carbonate matrix (transmitted light).

deep groundwater pathways of Oman hyperalkaline Ca-type springs, these springs randomly emanate from bedrock fissures unrelated to these tectonic structures, indicating that they follow other groundwater permeability pathways in the fissured aquifer. On the contrary, Mg-type spring waters generally follow tectonic contacts, emanating from fractured zones often associated with soils. The similar chemistry of meteoric-derived Mg-type spring waters and surface wadi waters (e.g. Paukert et al., 2012) suggests that they were both produced due to weathering processes taking place in the shallow serpentinized peridotite aquifer (Barnes and O'Neil, 1969; Dewandel et al., 2004).

The contrasting difference in the daily temperature fluctuations of Ca-type and Mg-type spring waters likely indicates that they are fed by groundwater from different depth horizons. The temperature of Ca-type hyperalkaline waters is rather constant (30–32 °C) and is likely indicative of deep groundwaters. The daily temperature of Mg-type spring waters fluctuates as much as 10–12 °C showing that they are fed from shallower groundwater horizons. The differences in temperature fluctuations support that, before their discharge, Ca-type and Mg-type waters probably circulate along distinct flow paths, and that their underground mixing was likely limited. Rempfert et al. (2017) argued, however, that subsurface mixing of both water types could be the cause for enhancing the chemical disequilibria that promotes the growth of some microbial communities in Oman Ophiolite deep aquifers. Although the chemical profile of Ca-type and Mg-type waters greatly differs, underground mixing—at least to some degree and at specific aquifer parts—is a possible scenario. Further research is needed to develop a better understanding of the pathways and processes controlling the groundwater circulation and mixing of both water types, and their impact on their chemistry and any potentially triggered precipitation.

5.2. Hydrodynamics, geochemistry and active precipitation in the Oman spring systems

The hydrology and hydrodynamics of the Oman spring systems are pivotal to understand the variations in the chemistry of Mix-type waters and the chemical, mineralogical, and textural characteristics of their mineral precipitates (Fig. 14). In the following subsections we discuss the various mineral phases and textures associated with the different water types, and how they are linked to the hydrological features and hydrodynamics characterizing the spring sites.

5.2.1. Hyperalkaline Ca-type waters

Deep-rooted Ca-type waters discharge—apparently scattered—throughout the spring sites, feeding regularly the pool waters with hyperalkaline waters upstream to downstream (Fig. 14). The depletion of Ca-type waters in DIC dictates atmospheric CO_2 uptake as one of the main contributors for carbonate precipitation. In addition, the slow Ca-type water flow rates (Q = 0.1–0.5 L s^{-}; Leleu et al., 2016) and the shallow nature of Ca-type pools promote evaporation under the arid climate conditions of Oman.

A thin (< 1 mm) crystalline crust on the water surface (Fig. 3A) is the main characteristic of hyperalkaline Ca-type waters. Crystalline crusts in Ca-type water pools and flow paths are mainly made of calcite (90–100 wt%; Table 6) that precipitates due to coupled effects of atmospheric CO_2 uptake and evaporation (e.g. Clark et al., 1992; Chavagnac et al., 2013b; Falk et al., 2016). The absence of Mg^{2+} ions and the low Mg/Ca ratio in Ca-type waters favor the precipitation of calcite (Folk, 1994; Pentecost, 2005), as well as the low dissolved CO_2 content (Fig. 11) inhibits aragonite precipitation (Jones, 2017a). In the

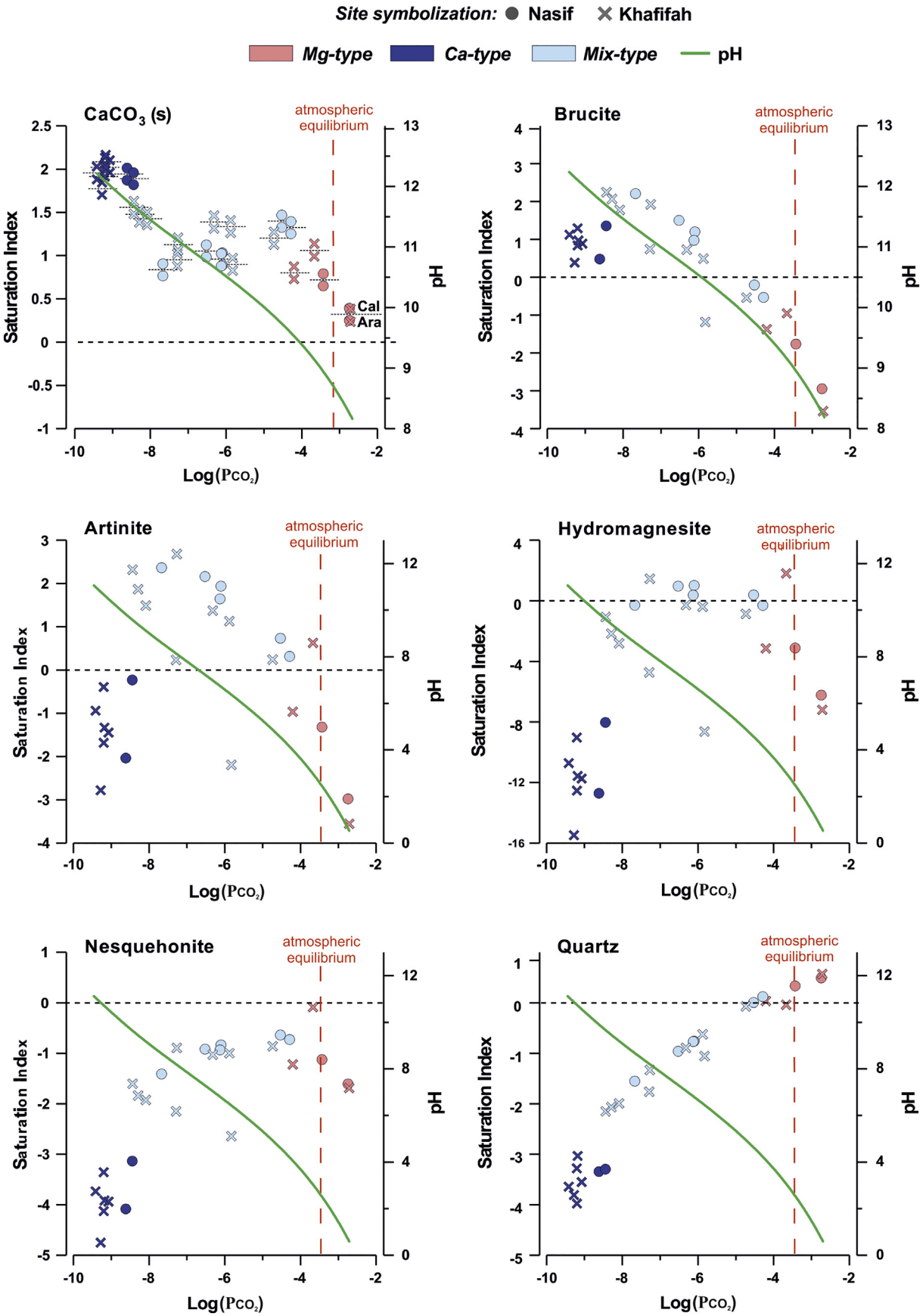

Fig. 11. Saturation index of potential mineral phases versus the Log(P_{CO2}) in the different water types of the two spring sites. The pH-curve in the diagrams (green line) is filled through actual data measured on-site. The $CaCO_3$ (s) diagram plots saturation index values for calcite (top-above the line) and aragonite (bottom-below the line) for each sample. (For interpretation of the references to color in this figure legend, the reader is referred to the web version of this article.)

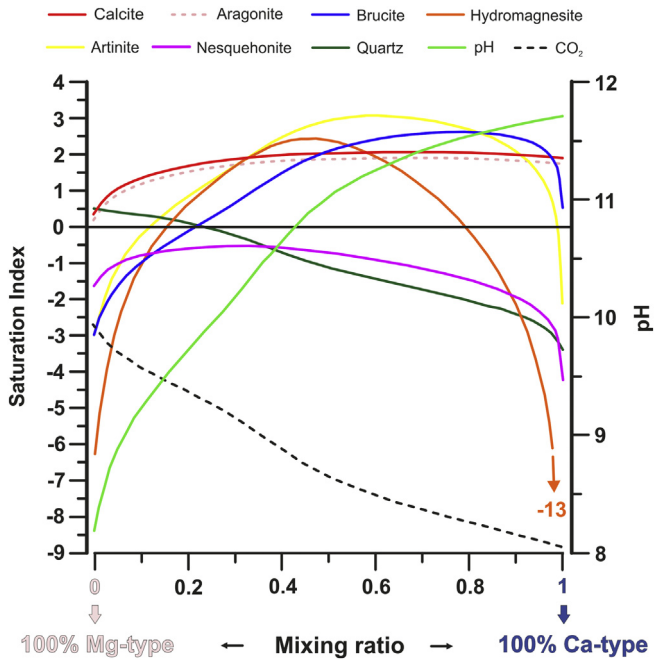

Fig. 12. Saturation index, pH, and CO_2 evolution during gradual mixing of Mg-type and Ca-type waters. Water sample OM15-1W was used as the end-member for pristine Mg-type waters and sample OM15-4W as the end-member for pristine Ca-type waters (see Table 2). The step of mixing ratios in the model is 0.01 (1%), starting from 100% Mg-type water (at 0 on the x axis) and ending up with a 100% Ca-type water (at 1 on the x axis).

absence of Mg ions, evaporation and CO_2 hydroxylation lead to extreme supersaturation rates and massive precipitation of calcite (Jones, 2017a, b). These fast supersaturation rates (Clark et al., 1992; Falk et al., 2016) in Ca-type waters could lead to the formation of initial calcite nuclei that remain attached to the air-water interface due to surface tension. This process may explain the presence of patches with small calcite crystals (< 4 μm) (Fig. 6B) in between the typical subhedral calcite crystals (up to 40 μm) in Ca-type crystalline crusts (Fig. 6A). Further evaporation in the pool can lead to high supersaturation and promote the observed precipitation of larger calcite crystals that use the initial small crystals as nucleation surface.

Evaporation of Ca-type waters produces a coating of precipitates on the rock around the pool rims (Fig. 3B). Similar to crystalline crusts, these rock coatings are calcite dominated (70–90 wt%; Table 6). The calcite crystals from rock coatings (Fig. 7D) and crystalline crusts (Fig. 6A) share similar sizes and morphologies that record the possible effects of evaporation on the textures of these sample types during precipitation. The curved edges of calcite crystals (Fig. 7D) are associated with high supersaturation (Gonzalez et al., 1992) with respect to calcium carbonate as a result of the high concentration of Ca^{2+} in the evaporating waters. Slow evaporation rates could lead to kinetically-controlled high-quality crystals (Jones, 2017bb), which is supported by the co-existence of euhedral {104} calcite crystals along with {120} calcite with curved edges and evident step-growth crystallization (Fig. 7D).

5.2.2. Mg-type and wadi waters

Unlike Ca-type waters, Mg-type waters are more scarce and less dispersed, often merging with surface wadi waters before mix with Ca-type waters. In most cases, the Mg-type and wadi waters (Q is up to 20 L s^{-1}) in the peridotites are perennial and their flow is higher than that of the Ca-type water (Dewandel et al., 2004). This constant water flow leads to influxes of large Mg-type water volumes in pool network, especially near the Mg-type spring outlets. The fraction of the Mg-type waters in the Mix-type waters decreases upstream to downstream, as the number of the Ca-type springs feeding the pool network increases.

The precipitation in Mg-type waters is limited including only rock coatings around the pool rims. Our study is the first report of broad occurrence of hydrated magnesium (hydroxy-) carbonates in the Oman Ophiolite Mg-type waters. Since most of the Oman Mg-type waters are undersaturated with respect to hydrated Mg-carbonate, evaporation is the most plausible factor controlling their precipitation. Hydrated magnesium (hydroxy-) carbonates are indicative of evaporative environments characterized by CO_2 degassing and high CO_2 content (e.g., Müller et al., 1972; Levy et al., 1999; Power et al., 2009; Power et al., 2019). Nesquehonite can be formed due to evapoconcentration around the Mg-type pools (Fig. 14) through cycles of recharge and subsequent evaporation of the pool waters. The large size (up to 2 mm) and the high quality of nesquehonite crystals in Mg-type waters (Fig. 7C) could indicate slow supersaturation rates, probably due to slow evaporation of the cooler Mg-type waters (Fig. S1Supplementary Material).

In the Khafifah spring site, one Mg-type water pool (i.e., OM15K–02W; Table 2) is supersaturated with respect to hydromagnesite (SI: 2) and artinite (SI: 0.8) (Fig. 11). The interaction of water with soil potentially accounts for its high Mg DIC concentration—that plays a crucial role in the precipitation of hydrated Mg-carbonates (Kloprogge et al., 2003; Ferrini et al., 2009; Power et al., 2019)—and favored the precipitation of hydrated Mg-carbonates (25 wt% nesquehonite and 70 wt% dypingite; Table 6). The XRD analysis showed that artinite in Mg-type pools is chlorartinite, a Cl-rich artinite variety, where OH^- is replaced by Cl^- in the crystal lattice. Co-precipitation of chlorartinite and nesquehonite is common in Cl^--rich evaporitic environments (Mignardi et al., 2011). Hydromagnesite only occurs in the Khafifah water pools with DIC > 5 mmol L^{-1}, attesting for precipitation in a CO_2-rich environment (Power et al., 2019).

Alternatively, the precipitation of hydrated Mg-carbonates may also be due to the increase of the OH^- concentration during the influx of Ca-type waters in Mg-type pools. In this scenario, evaporation would control nesquehonite precipitation, while the precipitation of dypingite, hydromagnesite, and artinite is governed by the pH increase (Zhang et al., 2006; Power et al., 2007) during Ca-type water influx events. These influx events could explain the observed transformation process of nesquehonite to dypingite in Fig. 16A, where a pseudomorph of dypingite forms after a prismatic crystal of nesquehonite. This could also imply a potential recharge of the pool with alkaline Mg-type waters. In both cases, the inserted fluid is undersaturated with respect to nesquehonite and initiates its dissolution. Subsequently, supersaturation with respect to dypingite or hydromagnesite could create an interfacial layer where the product mineral may take on the crystal morphology of the parent (pseudomorphic replacement; Fig. 16A) (Power et al., 2019 and references therein). This process is known as *interface-coupled dissolution-precipitation* (Ruiz-Agudo et al., 2014). In addition, the influence of Mg-type waters by Ca-type water influxes could introduce high amounts of OH^- in the pool leading to nesquehonite conversion into dypingite and/or hydromagnesite (Zhang et al., 2006; Power et al., 2007).

5.2.3. Mix-type waters

Massive Ca-carbonate deposits—mud-like precipitates and flocculent material—are systematically associated with Mix-type water pools, pointing that mixing of Ca-type and Mg-type waters is the primary cause for the precipitation of these deposits. Based on the stable isotope signature of Ca-carbonates, Falk et al. (2016) proposed that the main precipitation mechanisms of these deposits was both water mixing and atmospheric CO_2 uptake; however, Ca-carbonates with an atmospheric CO_2 uptake isotopic composition may have been formed in Ca-type pools and transported to the Mix-type pools by the water flow. Due to the relatively low SI of Ca-carbonate (SI: 0.6–1.; Fig. 11) in Mix-type waters—compared to other travertine forming environments (Pentecost, 2005; Leleu et al., 2016)—evaporation may have also played a role in the formation of these deposits.

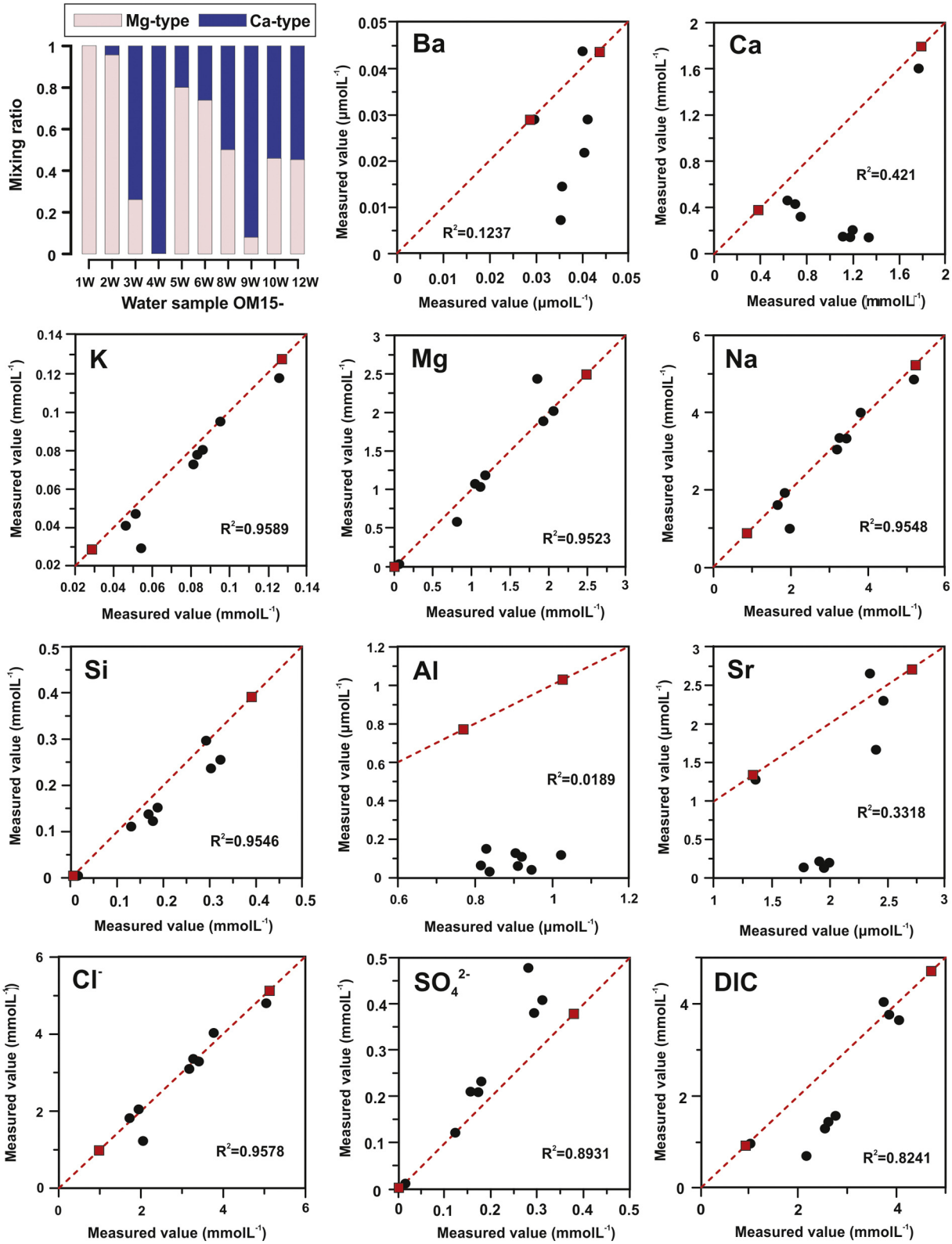

Fig. 13. Plots of measured (analytical) versus estimated (PHREEQC) concentrations using the collected water samples from the Nasif spring site. Water sample OM15-1W was used as the end-member for Mg-type waters and sample OM15-4W as the end-member for Ca-type waters (see Table 2). Red squares represent the values of the two end-members. The black circles correspond to the rest water samples. Red dashed line represents the indicative mixing trend. (For interpretation of the references to color in this figure legend, the reader is referred to the web version of this article.)

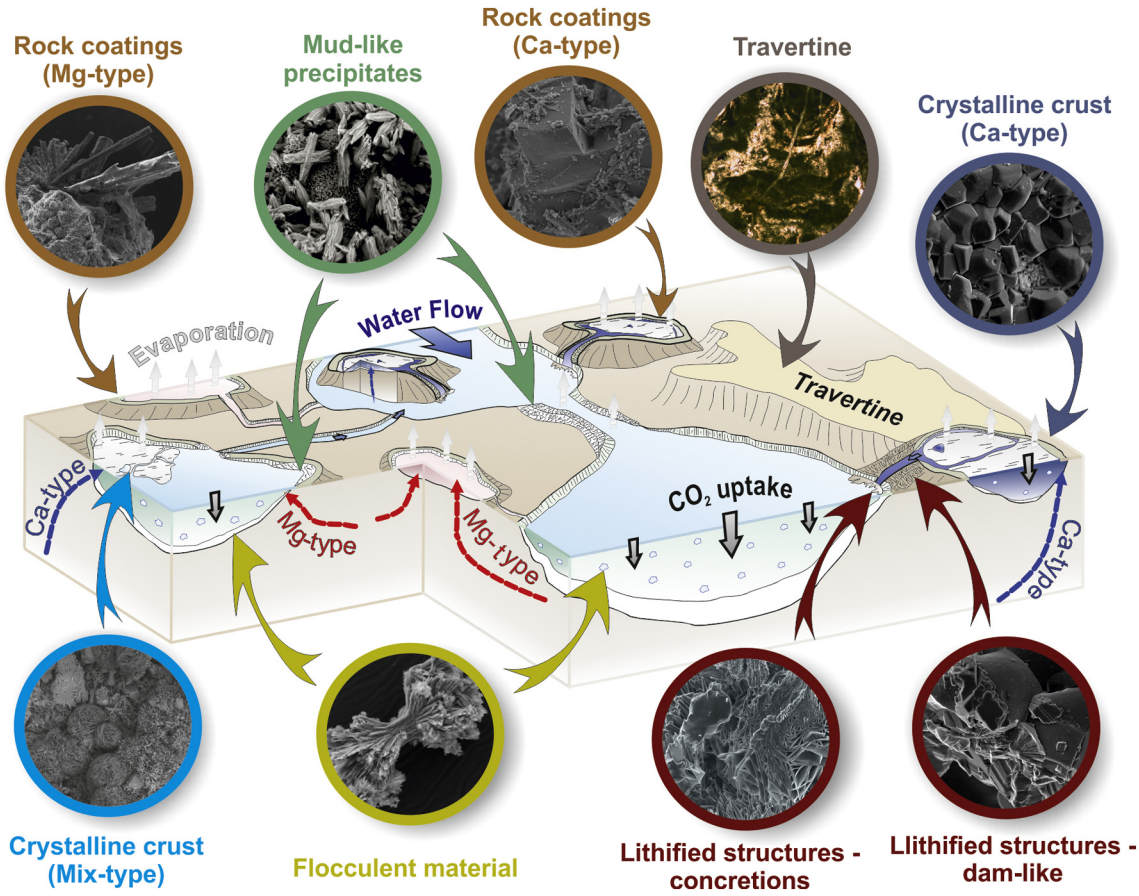

Fig. 14. Conceptual model of the Oman alkaline spring systems. The spring sites host different types of waters that are characterized by several types of precipitates with various textural characteristics. Water mixing, atmospheric CO_2 uptake, and evaporation are the main drivers of precipitation and textural differentiation of mineral phases occurring in the spring systems.

5.2.3.1. Mineralogy and textures of the precipitates in Mix-type waters. Aragonite is the dominant Ca-carbonate phase in Mix-type water pools due to the higher Mg concentration and Mg/Ca ratio relative to those in Ca-type waters (Table 6) (e.g. Falini et al., 1994; Pokrovsky, 1998; Lin and Singer, 2009; Chavagnac et al., 2013b, Jones, 2017aa, and references therein). In some cases, Mg-type and Ca-type waters discharge simultaneously into the same pool and create peculiar Mix-type pools (Fig. 14; e.g., OM15–03W). These Mix-type pools share a mixture of mineralogical and textural characteristics that reflects the strong influence of both Mg-type and Ca-type waters on mineral precipitation; aragonite–brucite (hydromagnesite)–calcite crystalline crusts (Table 3; OM15–03B–P) and aragonite–brucite (hydromagnesite)–calcite mud-like and flocculent material deposits (Table 3; OM15–03C–Pa) form, respectively, around Ca-type and of Mg-type water outlets (Fig. 14).

The texture of crystalline crusts in Mix-type waters is suggestive of an initial stage of aragonite nuclei formation that is followed by subsequent growth of the first crust segments at the air-water interface, likely caused by CO_2 uptake and evaporation (Fig. 15; Stage I). In a second stage (Fig. 15; Stage II), further growth of semi-spherical acicular aragonite takes place leading to the expansion of the crust. The growth of aragonite is unaffected by the presence of Mg ions, which remain —at least initially— in solution and suppress aragonite transformation into calcite (Berner, 1975; Reddy and Wang, 1980; Kitamura, 2001). The continuous growth of the crust leads to the development of an aragonitic layer that completely covers the water surface and becomes the substrate for later growth of brucite and calcite crystals (Fig. 15; Stage III). The development of the crystalline crust provides a non-turbulent environment and a physical substratum that promotes the growth of well-defined microplates of magnesium hydroxide, resulting in a better ordering of brucite crystals. In contact with atmospheric CO_2, brucite transforms to hydromagnesite, artinite or nesquehonite, what would account for the presence of hydromagnesite in some crystalline crusts (Fig. 6D) (Hostetler et al., 1966; Botha and Strydom, 2001; Simandl et al., 2008; Zhao et al., 2009). In the late crystallization stage (Fig. 15; Stage III), formation of brucite in the crystalline crusts decreases the Mg/Ca ratio of Mix-type waters, triggering the heterogeneous nucleation of calcite on the aragonitic crust surface. The euhedral shape of these crystals formed in this stage (Fig. 15) is indicative of slow crystal growth that was favored by the sluggish atmospheric CO_2 diffusion into water pools due to the formation of the crystalline crust (Chavagnac et al., 2013b; Olsson et al., 2014).

Aragonite particles from a single sample of flocculent material in Mix-type pools (Fig. 14) exhibits a large textural diversity (Fig. 8A) that reflects their formation under different supersaturation state and rates. The aragonite particle textures record an evolutionary path from an initial crystalline sheaf towards acicular, sphere-like aragonite (Fig. 16B). Higher supersaturation and faster supersaturation rates lead to aragonite formation that exhibits branching, displaying a splitting process at the growth front of the crystal (Rowling, 2004). This process creates fan-like morphologies at the tips of aragonite crystals that eventually form spherical aragonite morphologies (Fig. 16B) (Gránásy et al., 2005). Unlike mud-like precipitates, the aragonite textures in flocculent material record the changes in the values of supersaturation and supersaturation rates associated with environments of vigorous water mixing (e.g., in Mix-type pools where Mg-type and Ca-type waters discharge simultaneously) or rapid CO_2 uptake and evaporation

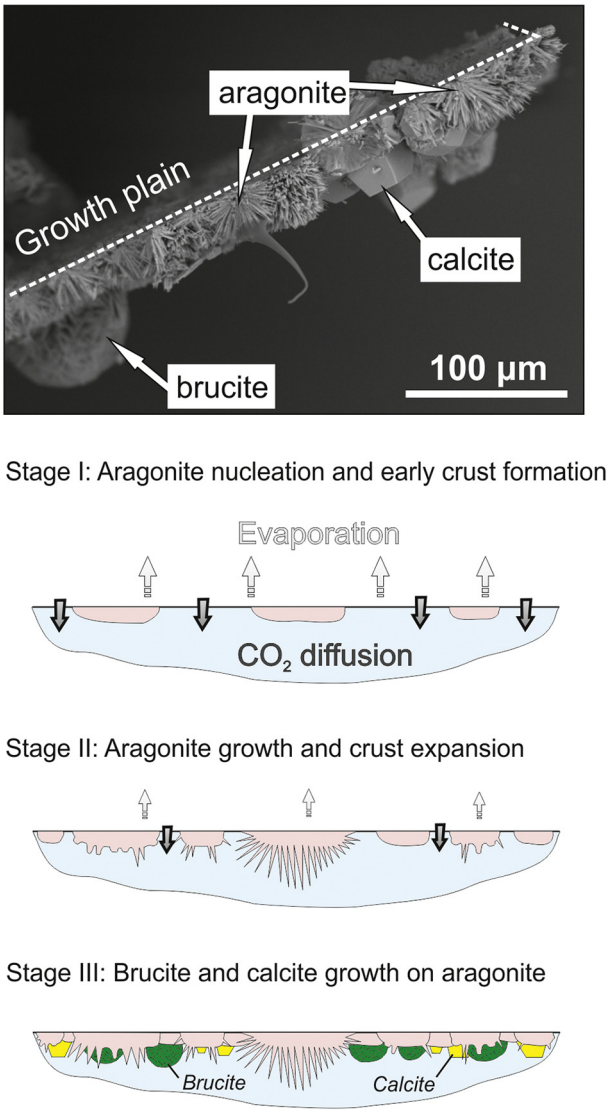

Fig. 15. The growth process of crystalline crusts in Mix-type waters. At initial crystallization stage, aragonite nucleates at the air-water interface due to evaporation and CO_2 uptake (Stage I). Further evaporation and CO_2 diffusion leads to aragonite growth and the development of the crystalline crust at the air-water interface (Stage II). Aragonite crystals act as a growth substrate for brucite and calcite formation, as well as a barrier for further CO_2 diffusion in the water (Stage III).

(e.g., near the air-water interface).

The deposition and development of dam-like formations (rippled terracing) is controlled by water hydrodynamics, in particular the bedrock morphology and local obstacles to the water flow paths (Hammer et al., 2007; Hammer et al., 2010) (Fig. 3D). Aragonite in dams (terraces) of mud-like precipitates show a self-organized nanocrystalline structure made of co-oriented nano-rods (Fig. 16C), suggesting nucleation and growth by accretion and not by classical crystal growth mechanisms. Diverging rod-made branches lead to wheat-sheaf shapes, whereas converging ones lead to spindle crystals with mesocrystalline structure (Fig. 16C). These structures could also be attributed to self-organization of aragonite mesocrystals, leading to crystals formed by crystalline subunits (Cölfen and Mann, 2003; Meldrum and Cölfen, 2008; Zhou et al., 2009; Jones, 2017b). The homogeneity of mineralogy (aragonite 63–100 wt%) and textures (Fig. 9A) in mud-like precipitates imply non variable saturation state and supersaturation rates. These steady conditions can be established in low energy environments of the pool networks, such as the mid-parts of shallow pools and the outmost parts of streams and pools. Indeed, these environments are the most common areas within the spring sites, where mud-like dams tend to form.

5.2.3.2. Brucite in Mix-type waters. Apart from crystalline crusts (see Section 5.2.3.1), brucite is uncommon in streams, but locally precipitates—occasionally forming brucite-bearing concretions (Fig. 3E)—in restricted mixing zones, where Ca-type waters come in contact with Mg-type and Mix-type waters (Fig. 14),. In these mixing zones, the water flow is slow, indicating the critical role of hydrodynamics on brucite occurrence. The relatively more energetic water flow of streams may prevent brucite settling and favor its dissolution (Chavagnac et al., 2013b), while mixing zones with slow water flow promotes the settling and/or preservation of brucite. The crystals of brucite in the concretions (Fig. 3E) display a distortion bending and a narrowing of the internal distances between the crystal flakes (Fig. 10B). These textural features likely indicate an on-going cementation process around mixing zones, where the hyperalkaline Ca-type waters come in contact with Mg-type or Mix-type waters under slow water flow conditions. At the parts of the concretions that aragonite growth is not inhibited by brucite, open-space crystallization of acicular, needle-like aragonite is favored (Fig. 10B).

Unlike Mix-type crystalline crusts, brucite crystals in mud-like and flocculent material (for frequency see Table 5) show smaller crystal sizes (< 5 µm) and lower degree of crystallinity (Fig. 8B) than brucite in the crystalline crusts (Fig. 6C). This textural feature is possibly indicative of faster supersaturation rates during vigorous mixing of Ca-type with Mg-type or Mg-rich Mix-type waters, where the steady supply of Mg^{2+} and OH^- keeps the water supersaturated with respect to brucite. In some cases, brucite occurs in mud-like and flocculent material from Mix-type water pools that are located away from mixing zones. This may indicate that brucite had formed elsewhere and was transported by the water flow in these pools. Nevertheless, according to our mixing model, the highest values of brucite supersaturation (SI: 2.5; Fig. 12) are attained where the Ca-type mixing fraction is between 0.5 and 0.9, which is in agreement with the Mix-type pools where brucite was actually found (Supplementary material Fig. 4S).

5.3. Development of travertine terraces

Preserved travertine terraces in Oman (Fig. 3F)—forming over the past 50,000 yrs (Mervine et al., 2014)—are extensive carbonate formations that mainly form via CO_2 uptake from the hyperalkaline Ca-type waters (Falk et al., 2016). In most cases, the travertine terraces develop in association with Ca-type springs and appear to have a close genetic relation to lithified dam-like structures (Fig. 3E).

Before reaching the final form of we observe today, the travertine terraces experience, early stages of cementation and lithification processes that can be observed in the lithified dam-like structures. Calcite exhibits internal lamination and undefined crystal boundaries (Fig. 10A) record the conversion of well-shaped crystals into the observed chaotic textures of the travertines. Similarly, aragonite structure is affected by the cementation processes and displays a compact texture by narrowing the space between the needle-like crystals (Fig. 10A). Compact textures of aragonite indicate its transformation into more stable calcite (Pentecost, 2005 and references within), which is the major component of Oman travertine terraces (Table 6). In some parts of these structures, calcite crystals exhibit concentric cavities, which often crosscut crystal boundaries (Fig. 3S, Supplementary material). These cavities on the calcite surfaces could be created by gas bubbles that are attached to the growth substrate (Aquilano et al., 2003; Taylor and Chafetz, 2004). Calcite starts forming on the bubble surface leaving an empty space at the place where the bubble was present. This kind of pores on calcite surface may also be associated with specific cellular functions (e.g., self-protection mechanisms, presence of polysaccharidic

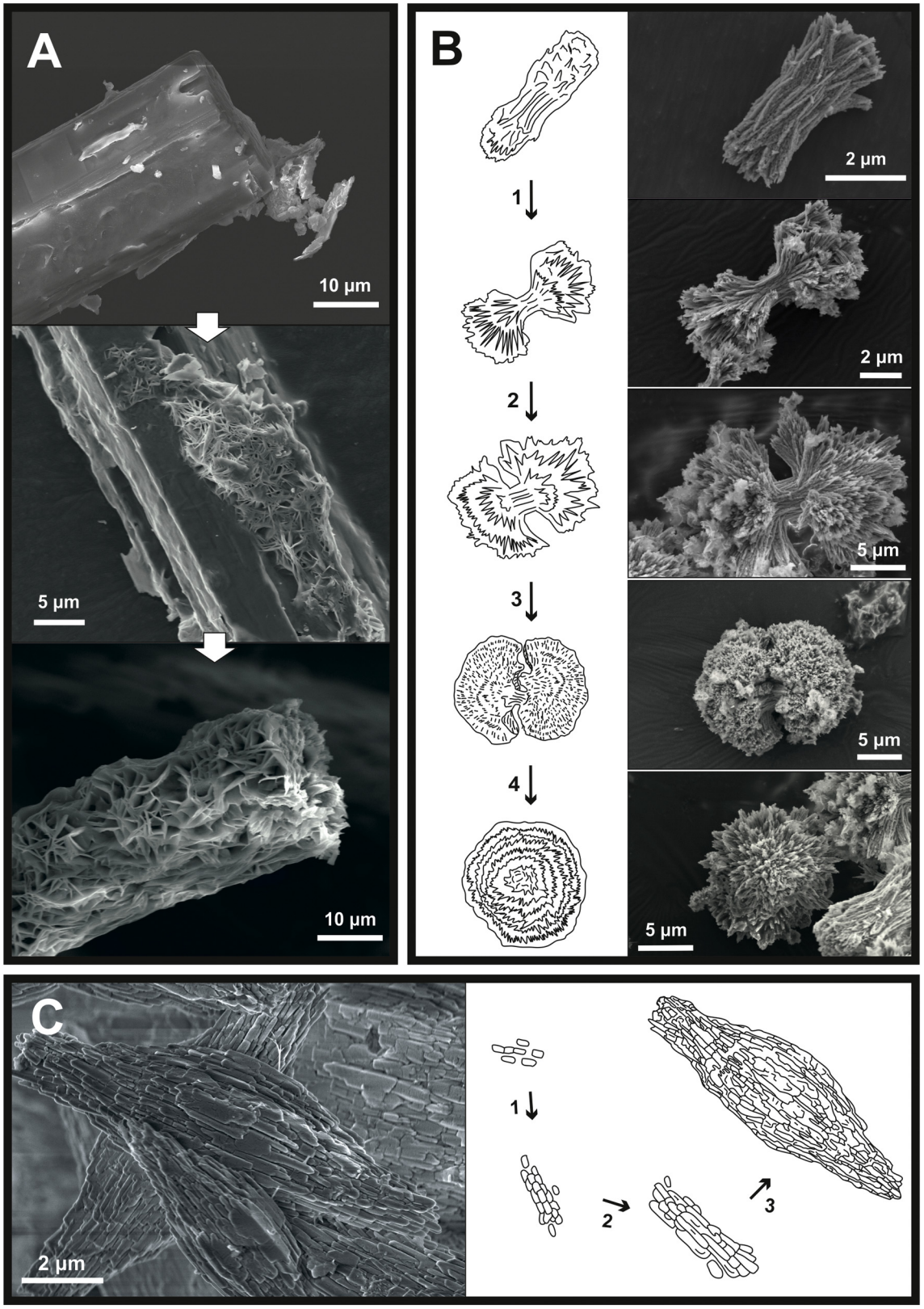

Fig. 16. SEM images and sketches describing the textural features and crystal growth processes of minerals occurring in the spring sites. A: The transformation process of nesquehonite into dypingite (pseudomorph crystal) in Mg-type waters. B: Branching and splitting processes lead to the textural evolution of aragonite in flocculent material from an initial crystalline sheaf, over wheat-sheaf and dumbbell, to an acicular-spheroidal morphology. C: Spindle aragonite crystals forming due to the aggregation of aragonite nano-rods via self-assembly processes.

capsule) processed byof several microbial communities (e.g., cyanobacteria) during calcium carbonate precipitation (Martinez et al., 2010; Bundeleva et al., 2014).

The lithified dam-like structures are exclusively associated with active Ca-type waters that run-off from Ca-type springs (Fig. 4; Fig. 14). The dominance of calcite over aragonite in these dam-like structures (Table 6) point to their precipitation directly from Ca-type waters without any indication of mixing with Mg-type waters. Alternations of active and inactive flow of Ca-type waters could trigger multiple recrystallization events that effect the development of the dam-like structures and subsequently the travertine terraces. Dehydration-hydration periods have an impact on calcite growth and reactivity (Fenter and Sturchio, 2012 and references within) that could lead to the chaotic and colloformic textures of the travertine terraces (Fig. 10C). Nevertheless, the strong presence of active carbonate precipitation due to mixing requires further assessment regarding its contribution and incorporation to the travertine terrace build-up.

6. Summary and conclusions

Interaction between meteoric water and ultramafic rocks in the Oman Ophiolite generates waters of variable physicochemical characteristics. The discharge of these waters forms complex hydrological networks of streams and pools where waters mix, undergo evaporation, and take up atmospheric CO_2, leading to the generation of a broad diversity of mineral phases and textures. Coupling of textural and mineralogical studies with chemical analysis of waters allowed us to determine the saturation state of a wide range of minerals and correlate them to the different water and precipitate types of the Oman spring sites. The systematic—downstream—sampling of numerous pools in individual spring sites, and the detailed documentation of mineral assemblages and crystal morphologies, enabled us to provide a more detailed account of how water composition, mixing, and mineral precipitation co-evolve in the alkaline spring systems. In accordance with previous studies, we classified the waters of the Oman spring sites into three types: Mg-type (mildly alkaline, $7.9 < pH < 9.5$; Mg^{2+}–HCO_3^--rich waters), Ca-type (hyperalkaline, $pH > 11.6$; Ca^{2+}–OH^--rich waters), and Mix-type waters (alkaline to hyperalkaline, $9.6 < pH < 11.5$; with intermediate chemical composition) formed by mixing of Mg-type and Ca-type.

The mineralogy and textures of different types of solid precipitates and deposits mostly record the local physicochemical characteristics of water, the hydrodynamic regime, and the evaporation rate of the spring sites. We first report the occurrence of hydrated magnesium (hydroxy-) carbonate phases in Oman Mg-type waters. Nesquehonite forms via evaporation and transforms into dypingite and hydromagnesite under locally CO_2-rich conditions. In Ca-type waters, coupled atmospheric CO_2 uptake and evaporation trigger the formation of calcitic crystalline crusts at the air-water interface, while the instantaneous mixing of Mg-type and Ca-type waters into a single Mix-water pool leads to the formation of aragonite-dominated and brucite-bearing crystalline crusts. In this type of Mix-water pools, acicular aragonite acts as a substrate for subsequent growth of brucite and calcite crystals. Throughout the spring sites, the Mix-type water pools also host massive aragonite-dominated deposits because the high Mg/Ca of these waters favors the formation of aragonite over calcite. The hydrodynamics of water mixing controls the occurrence of brucite, which is commonly restricted to mixing zones with steady mixing rate and slow water flow.

Crystal morphologies record the effect on the values of supersaturation and supersaturation rates in the pools due to mixing processes, evaporation and CO_2 uptake. In Ca-type waters, CO_2 uptake and evaporation dictate the textural characteristics of calcite both in crystalline crusts and rock coatings. Textural evolution of aragonite from initial crystalline sheaves to spheroidal shapes in flocculent material underlines the different supersaturation rates of calcium carbonate crystallization in Mix-type waters. Moreover, the spindle aragonite crystals in mud-like dam formations could be attributed to self-assembly processes via aggregation of nano-rod subunits. Mixing models between Mg-type and Ca-type waters revealed the evolution of mineral SIs under various mixing proportions and their relation to the observed mineral assemblages and chemistry of waters. Our results demonstrate that hydrology, geochemistry and local hydrodynamics characterizing the spring sites control the mineral assemblages, textures, and precipitation rate of the different types of solid precipitates occurring in the Oman alkaline spring systems.

Supplementary data to this article can be found online at https://doi.org/10.1016/j.chemgeo.2019.119435.

Declaration of competing interest

The authors declare that they have no known competing financial interests or personal relationships that could have appeared to influence the work reported in this paper.

Acknowledgements

We thank Francisca Espinosa Pérez, Manuel Jesús Román Alpiste for their help in fieldtrip logistics and technical support and, Cristobal Verdugo Escamilla for the X-ray analyses. We also thank Dr. Alfonso Garcia Caballero for scientific discussions. The present research has been funded by the European Union Seventh Framework Programme FP7/2007-2013 under the FP7 People Program (Marie Curie Action–ITN “Abyss”) under REA grant agreement no. 608001, and the F7 Ideas: European Research Council grant PROMETHEUS under grant agreement no. 340863.

References

Alt, J.C., Schwarzenbach, E.M., Früh-Green, G.L., Shanks, W.C., Bernasconi, S.M., Garrido, C.J., Crispini, L., Gaggero, L., Padrón-Navarta, J.A., Marchesi, C., 2013. The role of serpentinites in cycling of carbon and sulfur: seafloor serpentinization and subduction metamorphism. Lithos 178, 40–54.

Anraku, S., Morimoto, K., Sato, T., Yoneda, T., 2009. Formation of secondary minerals and uptake of various anions under naturally-occurring hyperalkaline conditions in Oman. In: ASME 2009 12th International Conference on Environmental Remediation and Radioactive Waste Management 2. Liverpool, UK, pp. 851–856.

Aquilano, D., Costa, E., Genovese, A., Massaro, F.R., Pastero, L., Rubbo, M., 2003. Hollow rhombohedral calcite crystals encompassing CO_2 microcavities nucleated in solution. J. Cryst. Growth 247, 516–522.

Bach, W., Paulick, H., Garrido, C.J., Ildefonse, B., Meurer, W.P., Humphris, S.E., 2006. Unraveling the sequence of serpentinization reactions: petrography, mineral chemistry, and petrophysics of serpentinites from MAR 15 N (ODP Leg 209, Site 1274). Geophys. Res. Lett. 33, L13306.

Barnes, I., La Marche, V.C., Himmelberg, G., 1967. Geochemical evidence of present-day serpentinization. Science 156, 830–832.

Barnes, I., O'Neil, J.R., 1969. The relationship between fluids in some fresh alpine-type ultramafics and possible modern serpentinization, western United States. Geol. Soc. Am. Bull. 80, 1947–1960.

Barnes, I., O'neil, J.R., Trescases, J.J., 1978. Present day serpentinization in New Caledonia, Oman and Yugoslavia. Geochim. Cosmochim. Acta 42, 144–145.

Barnes, I., Rapp, J.B., 1972. Metamorphic assemblages and the direction of flow of metamorphic fluids in four instances of serpentinization. Contrib. Mineral. Petrol. 35, 263–276.

Berner, R.A., 1975. The role of magnesium in the crystal growth of calcite and aragonite from seawater. Geochim. Cosmochim. Acta 39, 489–504.

Blank, J.G., Green, S.J., Blake, D., Valley, J.W., Kita, N.T., Treiman, A., Dobson, P.F., 2009. An alkaline spring system within the Del Puerto Ophiolite (California, USA): a Mars analog site. Planet. Space Sci. 57, 533–540.

Boschetti, T., Toscani, L., Iacumin, P., Selmo, E., 2017. Oxygen, hydrogen, boron and lithium isotope data of a natural spring water with an extreme composition: a fluid from the dehydrating slab? Aquat. Geochem. 23, 299–313.

Botha, A., Strydom, C.A., 2001. Preparation of a magnesium hydroxy carbonate from magnesium hydroxide. Hydrometallurgy 62, 175–183.

Boudier, F., Baronnet, A., Mainprice, D., 2010. Serpentine mineral replacements of natural olivine and their seismic implications: Oceanic lizardite versus subduction-related antigorite. J. Petrol. 51, 495–512.

Bruni, J., Canepa, M., Chiodini, G., Cioni, R., Cipolli, F., Longinelli, A., Marini, L., Ottonello, G., Zuccolini, M.V, 2002. Irreversible water–rock mass transfer accompanying the generation of the neutral, Mg–HCO3 and high-pH, Ca–OH spring waters of the Genova province, Italy. Appl. Geochem. 455–474.

Bundeleva, I.A., Shirokova, L.S., Pokrovsky, O.S., Bénézeth, P., Ménez, B., Gérard, E., Balor, S., 2014. Experimental modeling of calcium carbonate precipitation by

cyanobacterium Gloeocapsa sp. Chem. Geol. 374, 44–60.
Chavagnac, V., Monnin, C., Ceuleneer, G., Boulart, C., Hoareau, G., 2013a. Characterization of hyperalkaline fluids produced by low-temperature serpentinization of mantle peridotites in the Oman and Ligurian ophiolites. Geochem. Geophys. Geosyst. 14, 2496–2522.
Chavagnac, V., Ceuleneer, G., Monnin, C., Lansac, B., Hoareau, G., Boulart, C., 2013b. Mineralogical assemblages forming at hyperalkaline warm springs hosted on ultramafic rocks: a case study of Oman and Ligurian ophiolites. Geochem. Geophys. Geosyst. 14, 2474–2495.
Cipolli, F., Gambardella, B., Marini, L., Ottonello, G., Vetuschi, Zuccolini M., 2004. Geochemistry of high-pH waters from serpentinites of the Gruppo di Voltri (Genova, Italy) and reaction path modeling of CO_2 sequestration in serpentinite aquifers. Appl. Geochem. 19, 787–802.
Clark, I.D., Fontes, J.-C., Fritz, P., 1992. Stable isotope disequilibria in travertine from high pH waters: laboratory investigations and field observations from Oman. Geochim. Cosmochim. Acta 56, 2041–2050.
Coleman, R.G., 1981. Tectonic setting for ophiolite obduction in Oman. J. Geophys. Res. 86, 2497–2508.
Cölfen, H., Mann, S., 2003. Higher-order organization by mesoscale self-assembly and transformation of hybrid nanostructures. Angew. Chem. Inter. Ed. 42, 2350–2365.
Dasgupta, R., Hirschmann, M.M., 2010. The deep carbon cycle and melting in Earth's interior. Earth Planet. Sci. Lett. 298, 1–13.
de Gramont, X., Le Métour, J., Villey, M., 1986. Samad geologic map, sheet NF40-7C. In: Minist. of Commer. and Ind., Direct. Gen. of Miner., Muscat.
Dewandel, B., Lachassagne, P., Bakalowicz, M., Weng, P., Al-Malki A., 2003. Evaluation of aquifer thickness by analyzing recession hydrographs: application to the Oman ophiolite hard-rock aquifer. J. Hydrol. 274, 248–269.
Dewandel, B., Lachassagne, P., Qatan, A., 2004. Spatial measurements of stream baseflow, a relevant method for aquifer characterization and permeability evaluation: application to a hard rock aquifer, Oman ophiolite. Hydrol. Process. 18, 3391–3400.
Etiope, G., Vadillo, I., Whiticar, M.J., Marques, J.M., Carreira, P.M., Tiago, I., Benavente, J., Jiménez, P., Urresti, B., 2016. Abiotic methane seepage in the Ronda peridotite massif, southern Spain. Appl. Geochem. 66, 101–113.
Falini, G., Gazzano, M., Ripamonti, A., 1994. Crystallisation of calcium carbonate in presence of magnesium and polyelectrolytes. J. Cryst. Growth 137, 577–584.
Falk, E.S., Guo, W., Paukert, A.N., Matter, J.M., Mervine, E.M., Kelemen, P.B., 2016. Controls on the stable isotope compositions of travertine from hyperalkaline springs in Oman: insights from clumped isotope measurements. Geochim. Cosmochim. Acta 192, 1–28.
Fenter, P., Sturchio, N.C., 2012. Calcite (1 0 4)–water interface structure, revisited. Geochim. Cosmochim. Acta 97, 58–69.
Ferrini, V., De Vito, C., Mignardi, S., 2009. Synthesis of nesquehonite by reaction of gaseous CO_2 with Mg chloride solution: its potential role in the sequestration of carbon dioxide. J. Hazard. Mater. 168, 832–837.
Folk, R., 1994. Interaction between bacteria, nannobacteria, and mineral precipitation in hot springs of central Italy. Géographie Physique et Quaternaire 48, 233–246.
Frost, B.R., Beard, J.S., 2007. On silica activity and serpentinization. J. Petrol. 48, 1351–1368.
García-Ruiz, J.M., Hyde, S.T., Carnerup, A.M., Christy, A.G., Van Kranendonk, M.J., Welham, N.J., 2003. Self-assembled silica-carbonate structures and detection of ancient microfossils. Science 302, 1194–1197.
García-Ruiz, J.M., Nakouzi, E., Kotopoulou, E., Tamborrino, L., Steinbock, O., 2017. Biomimetic mineral self-organization from silica-rich spring waters. Sci. Adv. 3 (p. e 1602285).
Giampouras, M., Garrido, C.J., Zwicker, J., Vadillo, I., Smrzka, D., Bach, W., Peckmann, J., Jiménez, P., Benavente, J., García-Ruiz, J.M., 2020. Geochemistry and mineralogy of serpentinization-drivenhyperalkaline springs in the Ronda peridotites. Lithos. https://doi.org/10.1016/j.lithos.2019.105215.
Glennie, K.W., Bouef, M.G.A., Hughes-Clark, M.W., Moody-Stuart, M., Pilaar, W.F.H., Reinhardt, B.M., 1973. Late Cretaceous nappes in the Oman mountains and their geological evolution. Am. Assoc. Pet. Geol. Bull. 57, 5–27.
Godard, M., Jousselin, D., Bodinier, J.L., 2000. Relationships between geochemistry and structure beneath a palaeo-spreading centre: a study of the mantle section in the Oman ophiolite. Earth Planet. Sci. Lett. 180, 133–148.
Godard, M., Dautria, J.M., Perrin, M., 2003. Geochemical variability of the Oman ophiolite lavas: relationship with spatial distribution and paleomagnetic directions. Geochem. Geophys. Geosyst. 4, 8609.
Gonzalez, L.A., Carpenter, S.J., Lohmann, K.C., 1992. Inorganic calcite morphology; roles of fluid chemistry and fluid flow. J. Sediment. Res. 62, 382–399.
Gránásy, L., Pusztai, T., Tegze, G., Warren, J.A., Douglas, J.F., 2005. Growth and form of spherulites. Phys. Rev. 72, 11605.
Hammer, Ø., Dysthe, D.K., Jamtveit, B., 2007. The dynamics of travertine dams. Earth Planet. Sci. Lett. 256, 258–263.
Hammer, Ø., Dysthe, D.K., Jamtveit, B., 2010. Travertine terracing: patterns and mechanisms. J. Geol. Soc. 336, 345–355.
Hanghøj, K., Kelemen, P.B., Hassler, D., Godard, M., 2010. Composition and genesis of depleted mantle peridotites from the Wadi Tayin Massif, Oman Ophiolite; major and trace element geochemistry, and Os isotope and PGE systematics. J. Petrol. 51, 201–227.
Hostetler, P.B., Coleman, R.G., Mumpton, F.A., 1966. Brucite in alpine serpentinites. Am. Mineral. 51, 75–98.
Jones, B., 2017a. Review of calcium carbonate polymorph precipitation in spring systems. Sediment. Geol. 353, 64–75.
Jones, B., 2017b. Review of aragonite and calcite crystal morphogenesis in thermal spring systems. Sediment. Geol. 354, 9–23.
Kelemen, P.B., Manning, C.E., 2015. Reevaluating carbon fluxes in subduction zones, what goes down, mostly comes up. Proc. Natl. Acad. Sci. U. S. A. 112, E3997–E4006.
Kelemen, P.B., Matter, J.M., 2008. In situ carbonation of peridotite for CO_2 storage. Proc. Natl. Acad. Sci. U. S. A. 105, 17295–17300.
Kelemen, P.B., Matter, J.M., Streit, E.E., Rudge, J.F., Curry, W.B., Blusztajn, J., 2011. Rates and mechanisms of mineral carbonation in peridotite: natural processes and recipes for enhanced, in situ CO_2 capture and storage. Annu. Rev. Earth Planet. Sci. 39, 545–576.
Kelley, D.S., Karson, J.A., Blackman, D.K., Früh-Green, G.L., Butterfield, D.A., Lilley, M.D., Olson, E.J., Schrenk, M.O., Roe, K.K., Lebon, G.T., Rivizzigno, P., 2001. An off-axis hydrothermal vent field near the Mid-Atlantic Ridge at 30 N. Nature 412, 145–149.
Kelley, D.S., Karson, J.A., Früh-Green, G.L., Yoerger, D.R., Shank, T.M., Butterfield, D.A., Hayes, J.M., Schrenk, M.O., Olson, E.J., Proskurowski, G., Jakuba, M., Bradley, A., Larson, B., Ludwig, K., Glickson, D., Buckman, K., Bradley, A.S., Brazelton, W.J., Roe, K., Elend, M.J., Delacour, A., Bernasconi, S.M., Lilley, M.D., Baross, J.A., Summons, R.E., Sylva, S.P., 2005. A serpentinite-hosted ecosystem: the Lost City hydrothermal field. Science 307, 1428–1434.
Kitamura, M., 2001. Crystallization and transformation mechanism of calcium carbonate polymorphs and the effect of magnesium ion. J. Colloid. Interface Sci. 236, 318–327.
Klein, F., Garrido, C.J., 2011. Thermodynamic constraints on mineral carbonation of serpentinized peridotite. Lithos 126, 147–160.
Klein, F., Bach, W., Jöns, N., McCollom, T., Moskowitz, B., Berquó, T., 2009. Iron partitioning and hydrogen generation during serpentinization of abyssal peridotites from 15 N on the Mid-Atlantic Ridge. Geochim. Cosmochim. Acta 73, 6868–6893.
Kloprogge, J.T., Martens, W.N., Nothdurft, L., Duong, L.V., Webb, G.E., 2003. Low temperature synthesis and characterization of nesquehonite. J. Mater. Sci. Lett. 22, 825–829.
Lane, N., Martin, W., 2010. The energetics of genome complexity. Nature 467, 929.
Leleu, T., Chavagnac, V., Delacour, A., Noiriel, C., Ceuleneer, G., Aretz, M., Rommevaux, C., Ventalon, S., 2016. Travertines Associated With Hyperalkaline Springs: Evaluation As A Proxy For Paleoenvironmental Conditions And Sequestration of Atmospheric CO_2. J. Sediment. Res. 86, 1328–1343.
Levy, D.B., Schramke, J.A., Esposito, K.J., Erickson, T.A., Moore, J.C., 1999. The shallow ground water chemistry of arsenic, fluorine, and major elements: Eastern Owens Lake, California. Appl. Geochem. 14, 53–65.
Lin, Y.P., Singer, P.C, 2009. Effect of Mg2+ on the kinetics of calcite crystal growth. J. Cryst. Growth 312, 136–140.
Lippard, S.J., Shelton, A.W., Gass, I.G., 1986. The ophiolite of Northern Oman. Published for The Geological Society by Blackwell Scientific Publications.The ophiolite of Northern Oman. Published for The Geological Society by Blackwell Scientific Publications.
Ludwig, K.A., Kelley, D.S., Butterfield, D.A., Nelson, B.K., Früh-Green, G., 2006. Formation and evolution of carbonate chimneys at the Lost City Hydrothermal Field. Geochim. Cosmochim. Acta 70, 3625–3645.
Martin, W., Russell, M.J., 2007. On the origin of biochemistry at an alkaline hydrothermal vent. Philos. Trans. R. Soc. Lond. Ser. B Biol. Sci. 362, 1887–1926.
Marques, J.M., Carreira, P.M., Carvalho, M.R., Matias, M.J., Goff, F.E., Basto, M.J., Graça, R.C., Aires-Barros, L., Rocha, L., 2008. Origins of high pH mineral waters from ultramafic rocks, Central Portugal. Appl. Geochem. 23, 3278–3289.
Martin, W., Baross, J., Kelley, D., Russell, M.J., 2008. Hydrothermal vents and the origin of life. Nat. Rev. Microbiol. 6, 805.
Martinez, R.E., Gardés, E., Pokrovsky, O.S., Schott, J., Oelkers, E.H., 2010. Do photosynthetic bacteria have a protective mechanism against carbonate precipitation at their surfaces? Geochim. Cosmochim. Acta 74, 1329–1337.
Matter, J.M., Kelemen, P.B., 2009. Permanent storage of carbon dioxide in geological reservoirs by mineral carbonation. Nat. Geosci. 2, 837–841.
Meldrum, F., Cölfen, H., 2008. Controlling mineral morphologies and structures in biological and synthetic systems. Chem. Rev. 108, 4332–4432.
Menzel, M.D., Garrido, C.J., López Sánchez-Vizcaíno, V., Marchesi, C., Hidas, K., Escayola, M.P., Delgado Huertas, A., 2018. Carbonation of mantle peridotite by CO_2-rich fluids: the formation of listvenites in the Advocate ophiolite complex (Newfoundland, Canada). Lithos 323, 238–261.
Menzel, M.D., Garrido, C.J., Sánchez-Vizcaíno, V.L., Hidas, K., Marchesi, C., 2019. Subduction metamorphism of serpentinite-hosted carbonates beyond antigorite serpentinite dehydration (Nevado-Filábride Complex, Spain). J. Metamorph. Geol. 37, 681–715.
Mervine, E.M., Humphris, S.E., Sims, K.W., Kelemen, P.B., Jenkins, W.J., 2014. Carbonation rates of peridotite in the Samail Ophiolite, Sultanate of Oman, constrained through ^{14}C dating and stable isotopes. Geochim. Cosmochim. Acta 126, 371–397.
Mignardi, S., De Vito, C., Ferrini, V., Martin, R.F., 2011. The efficiency of CO_2 sequestration via carbonate mineralization with simulated wastewaters of high salinity. J. Hazard. Mater. 191, 49–55.
Miller, H.M., Matter, J.M., Kelemen, P., Ellison, E.T., Conrad, M.E., Fierer, N., Ruchala, T., Masako, T., Templeton, A.S., 2016. Modern water/rock reactions in Oman hyperalkaline peridotite aquifers and implications for microbial habitability. Geochim. Cosmochim. Acta 179, 217–241.
Monnier, C., Girardeau, J., Le Mée, L., Polvé, M., 2006. Along-ridge petrological segmentation of the mantle in the Oman ophiolite. Geochem. Geophys. Geosyst. 7, Q11008.
Monnin, C., Chavagnac, V., Boulart, C., Ménez, B., Gérard, M., Gérard, E., Pisapia, C., Quéméneur, M., Erauso, G., Postec, A., Guentas-Dombrowski, L., Payri, C., Pelletier, B., 2014. Fluid chemistry of the low temperature hyperalkaline hydrothermal system of Prony Bay (New Caledonia). Biogeosciences 11, 5687.
Morrill, P.L., Kuenen, J.G., Jonhson, O.G., Suzuki, S., Rietze, A., Sessions, A.L., Fogel, M.L., Nealson, K.H., 2013. Geochemistry and geobiology of a present-day

serpentinization site in California: The Cedars. Geochim. Cosmochim. Acta 109, 222–240.
Müller, G., Irion, G., Förstner, U., 1972. Formation and diagenesis of inorganic Ca–Mg carbonates in the lacustrine environment. Naturwissenschaften 59, 158–164.
Neal, C., Shand, P., 2002. Spring and surface water quality of the Cyprus ophiolites. Hydrol. *Earth Syst. Sci.* 6, 797–817.
Neal, C., Stanger, G., 1983. Hydrogen generation from mantle source rocks in Oman. Earth Planet. Sci. Lett. 66, 315–320.
Neal, C., Stanger, G., 1984. Calcium and magnesium hydroxide precipitation from alkaline groundwaters in Oman, and their significance to the process of serpentinization. Mineral. Mag. 48, 237–241.
Neal, C., Stanger, G., 1985. Past and present serpentinization of ultramafic rocks: an example from the Semail ophiolite nappe of northern Oman. In: Drewer, J.I. (Ed.), The Chemistry of Weathering. D. Reidel Publishing Company, Holland, pp. 249–275.
Nicolas, A., Boudier, F., Ildefonse, V., Ball, E., 2000. Accretion of Oman and United Arab Emirates ophiolite—discussion of a new structural map. Mar. Geophys. Res. 21, 147–149.
Olsson, J., Stipp, S.L.S., Gislason, S.R., 2014. Element scavenging by recently formed travertine deposits in the alkaline springs from the Oman Semail Ophiolite. Min. Mag. 78, 1479–1490.
Palandri, J.L., Reed, M.H., 2004. Geochemical models of metasomatism in ultramafic systems: serpentinization, rodingitization, and sea floor carbonate chimney precipitation. Geochim. Cosmochim. Acta 68, 1115–1133.
Parkhurst, D.L., Appelo, C.A.J., 1999. User's guide to PHREEQC (version 2): a computer program for speciation, batch-reaction, one-dimensional transport, and inverse geochemical calculations. In: US Geol. Survey Water Resour. Invest. Rep. 99. pp. 312.
Paukert, A.N., Matter, J.M., Kelemen, P.B., Shock, E.L., Havig, J.R., 2012. Reaction path modeling of enhanced in situ CO2 mineralization for carbon sequestration in the peridotite of the Samail Ophiolite, Sultanate of Oman. Chem. Geol. 330–331, 86–100.
Pentecost, A., 2005. Travertine. Springer-Verlag, Berlin.
Pokrovsky, O.S., 1998. Precipitation of calcium and magnesium carbonates from homogeneous supersaturated solutions. J. Cryst. Growth 186, 233–239.
Power, I.M., Wilson, S.A., Thom, J.M., Dipple, G.M., Southam, G., 2007. Biologically induced mineralization of dypingite by cyanobacteria from an alkaline wetland near Atlin, British Columbia, Canada. Geochem. Trans. 8, 13.
Power, I.M., Wilson, S.A., Thom, J.M., Dipple, G.M., Gabites, J.E., Southam, G., 2009. The hydromagnesite playas of Atlin, British Columbia, Canada: a biogeochemical model for CO_2 sequestration. Chem. Geol. 260, 286–300.
Power, I.M., Harrison, A.L., Dipple, G.M., Wilson, S.A., Barker, S.L., Fallon, S.J., 2019. Magnesite formation in playa environments near Atlin, British Columbia, Canada. Geochim. Cosmochim. Acta 255, 1–24.
Proskurowski, G., Lilley, M.D., Kelley, D.S., Olson, E.J., 2006. Low temperature volatile production at the Lost City Hydrothermal Field, evidence from a hydrogen stable isotope geothermometer. Chem. Geol. 229, 331–343.
Reddy, M.M., Wang, K.K., 1980. Crystallization of calcium carbonate in the presence of metal ions: I. Inhibition by magnesium ion at pH 8.8 and 25 C. J. Cryst. Growth 50, 470–480.
Rempfert, K.R., Miller, H.M., Bompard, N., Nothaft, D., Matter, J.M., Kelemen, P., Fierer, N., Templeton, A.S., 2017. Geological and geochemical controls on subsurface microbial life in the Samail Ophiolite, Oman. Front. Microbiol. 8, 56.
Rietveld, H., 1969. A profile refinement method for nuclear and magnetic structures. J. Appl. Crystallogr. 2, 65–71.
Rowling, J., 2004. Studies on aragonite and its occurrence in caves, including New South Wales caves. J. proc. R. Soc. N.S.W. 137, 123–149.
Ruiz-Agudo, E., Putnis, C.V., Putnis, A., 2014. Coupled dissolution and precipitation at mineral–fluid interfaces. Chem. Geol. 383, 132–146.
Sánchez-Murillo, R., Gazel, E., Schwarzenbach, E.M., Crespo-Medina, M., Schrenk, M.O., Boll, J., Gill, B.C., 2014. Geochemical evidence for active tropical serpentinization in the Santa Elena Ophiolite, Costa Rica: an analog of a humid early Earth? Geochem. Geophys. Geosyst. 15, 1783–1800.
Schrenk, M.O., Brazelton, W.J., Lang, S.Q., 2013. Serpentinization, carbon, and deep life. Rev. Mineral. Geochem. 75, 575–606.
Searle, M.P., Cox, J., 2002. Subduction zone metamorphism during formation and emplacement of the Semail ophiolite in the Oman Mountains. Geol. Mag. 139, 241–255.
Seifritz, W., 1990. CO_2 disposal by means of silicates. Nature 345, 486.
Simandl, G.J., Paradis, S., Irvine, M., 2008. Brucite–uses, exploration guidelines and selected grass-root exploration targets. Can. Inst. Min. Bull. 101, 1–7.
Sleep, N.H., Bird, D.K., Pope, E.C., 2011. Serpentinite and the dawn of life. Philos. Trans. R. Soc. Lond. Ser. B Biol. Sci. 366, 2857–2869.
Stanger, G., 1986. The Hydrogeology of the Oman Mountains. Ph. D. thesis. Department of Earth Sciences, The Open University, U.K.
Streit, E., Kelemen, P., Eiler, J., 2012. Coexisting serpentine and quartz from the carbonate bearing serpentinized peridotite in the Samail Ophiolite, Oman. Contrib. Mineral. Petrol. 164, 82–837.
Stumm, W., Morgan, J.J., 1996. Aquatic Chemistry: Chemical Equilibria and Rates in Natural Waters. Wiley.
Szponar, N., Brazelton, W.J., Schrenk, M.O., Bower, D.M., Steele, A., Morrill, P.L., 2013. Geochemistry of a continental site of serpentinization, the Tablelands Ophiolite, Gros Morne National Park: A Mars analogue. Icarus. 224. pp. 286–296.
Taylor, P.M., Chafetz, H.S., 2004. Floating rafts of calcite crystals in cave pools, central Texas, USA: crystal habit vs. saturation state. J. Sediment. Res. 74, 328–341.
Yuce, G., Italiano, F., D'Alessandro, W., Yalcin, T.H., Yasin, D.U., Gulbay, A.H., Ozyurt, N.N., Rojay, B., Karabacak, V., Bellomo, S., Brusca, L., Yang, T., Fu, C.C., Lai, C.W., Ozacar, A., Walia, V., 2014. Origin and interactions of fluids circulating over the Amik Basin (Hatay, Turkey) and relationships with the hydrologic, geologic and tectonic settings. Chem. Geol. 388, 23–39.
Zhang, Z., Zheng, Y., Ni, Y., Liu, Z., Chen, J., Liang, X., 2006. Temperature-and pH-dependent morphology and FT–IR analysis of magnesium carbonate hydrates. J. Phys. Chem. B 110, 12969–12973.
Zhao, L., Sang, L., Chen, J., Ji, J., Teng, H.H., 2009. Aqueous carbonation of natural brucite: relevance to CO_2 sequestration. Environ. Sci. Technol. 44, 406–411.
Zhou, G.T., Yao, Q.Z., Ni, J., Jin, G., 2009. Formation of aragonite mesocrystals and implication for biomineralization. Am. Mineral. 94, 293–302.